ELSEVIER

Coordination Chemistry Reviews
178–180 (1998) 1109–1163

COORDINATION CHEMISTRY REVIEWS

Retrosynthesis in inorganic crystal structures: application to nesosilicate and inosilicate networks

Marc Henry *

Laboratoire de Chimie Moléculaire de l'Etat Solide, Université Louis Pasteur, Institut Le Bel, 4, Rue Blaise Pascal, 67070 Strasbourg, Cedex, France

Received 15 December 1997; accepted 16 June 1998

Contents

---

* Corresponding author. Tel.: +33 3 88415313; Fax: +33 3 88415313; e-mail: henry@chimie.u-strasbg.fr

PII S0010-8545(98)00167-2

Abstract

This paper presents the use of a retrosynthetic tool allowing one to reduce any crystalline structure to a set of two or three simple chemical "tectons" from which the whole network may be reconstituted. This reduction is performed by probing the susceptibility of any finite secondary building unit to the removal of translation symmetry operators. Atoms displaying atomic charge invariance upon extraction from the network are assumed to belong to the chemical tectons which are at the origin of crystalline growth from molecular species. The chemical bond pattern found around these structural "corner-stones" defines small groups of polyhedra sharing corners or edges and whose topologies are easily understandable in terms of the well-known coordination chemistry of the cationic centers involved. The paper is divided into two parts. The first part is a review of the basic chemical reactions allowing the sharing of corners between two coordination polyhedra from a kinetic point of view. The second part describes the retrosyntheses of about 50 crystalline structures displaying either insular groups (nesosilicates) or chains (inosilicates) of SiO_4 tetrahedra. This study shows that hydrogen bonding with solvent molecules provides a few eV of stabilization for an anionic species against a few tens eV for hydrogen bonding with a solvated cation and a few hundreds eV for direct interaction with a naked cation. Tectons which have emerged from a careful analysis of the selected crystalline structures are uncomplexed linear oligomers (SiO_4, Si_2O_7 Si_3O_{10}), uncomplexed metasilicate rings (Si_3O_9, Si_4O_{12}, Si_6O_{18}) and complexed linear oligomers ($TiSiO_4$, $SbSiO_4$, $Mn_2Si_2O_7$, $Mn_3Si_3O_{10}$, $Mn_3Si_3O_{10}$, $SiBeAlO_{10}$, $Si_2Be_2O_{13}$). Some phases cannot yet be studied owing to the non-localization of hydrogen atoms or to the occurence of cationic disorder. The failure to detect any linear oligomer Si_nO_{3n+1} with $n>4$ or huge Si_nO_{3n} rings ($n>9$) in solution or in the solid state has been clearly interpreted as the consequence of very unfavorable electrostatic balances for these species. Our observation that such a wide range of silicated crystal structures can be analyzed using just monomeric, dimeric, trimeric or tetrameric tectons is a very encouraging result for future investigations of fully reticulated three-dimensional (3D) networks such as those found in microporous compounds.

Keywords: Retrosynthesis; Nesosilicate networks; Inosilicate networks

1. Introduction

Designing high-tech solid materials is the challenge that solid-state chemists have to take up at the dawn of the third millenium. For thousand of years, solid-state chemistry was the art of breaking down solids at high temperatures in order to force them to react together at an acceptable rate. At the very end of the twentieth century, the glass and ceramics industries still rely heavily on grinders and furnaces, whereas wet processes involving flasks, beakers or autoclaves with temperatures not higher than 300 °C are routinely used at the laboratory scale [1–3]. On moving from dry to wet chemistry, solid-state scientists discovered a completely new soft and sticky world, and coined the name "sol–gel chemistry" in the early 1980s to cover this new field of research [4,5]. The principle of all sol–gel syntheses is to start from molecular or nanoscopic-sized compounds in solution and to play with all their physicochemical interactions (van der Waals or dipolar forces, hydrogen bonding, coordination links, iono-covalent bonding, etc.) with the aim of obtaining a tailor-made solid-state material. In this solid-state quest, chemists have to struggle against numerous illdefined colloidal states of matter, relying heavily on spectroscopic methods to trace the destiny of their starting precursors [6,7]. This is not an easy task. At a mesoscopic scale, colloids can have their own chemical structure, often extremely different from the well-defined structures found at both the nanoscopic (molecule or cluster) or macroscopic (crystalline solid) ends. Another problem is that the most active species in the crystal growth process are those with the lowest concentrations. Consequently, most analytical tools miss them completely, focussing on dead ends which are not reactive enough to participate directly in crystal growth. However, owing to the well-known chemical equilibrium rules, these dead-end compounds regulate the concentration of every species present in the solution and may have a deep influence, not on the crystalline structure itself, but rather on the crystal size and morphology [8]. Despite these intrinsic difficulties, the use of sol–gel syntheses in solid-state chemistry is quite rewarding. As elaboration temperatures rise and fall, chemical reactions progressively lose their leveling entropic heaviness to gain all the enthalpic delicacy and flexibility of solution chemistry. Incredible and amazing crystal structures can thus be extracted from the solution, not just by changing the temperature, pH or ionic strength, but also by playing with the solvent composition or its structure through the use of chemical additives [9–11]. Faced with such a tremendous amount of new phases, it becomes more and more difficult to speak of purely organic or inorganic chemical objects. The term “hybrid materials” has thus be coined in the 1990s to describe reticulated networks ranging from organic polymers bearing inorganic bridges to organically grafted inorganic materials, quite often showing very original properties [12]. The formation in solution of these new materials raises some fascinating, still unanswered, questions: what is a building block? Is there a limit to the size of a building block in solution? Given the structure of a building block, how many reactive sites can be identified for chemical attacks, and what is the relative order of their reactivity? Can we chemically design some building blocks which, through an iterative auto-assembling process deep-rooted in their chemical structure, will lead three-dimensional (3D) frameworks with complete control of both structure and texture?

It is the aim of this paper to begin to answer these fundamental questions. In the following we will focus not on the sol–gel syntheses of new phases, nor on the practical applications of these phases, but rather on trying to check whether the building block concept itself is chemically sound. In molecular chemistry (either organic or inorganic), this action of reducing a chemical object to its ultimate constituents from which the whole molecule can be synthesized is called retrosynthesis [13]. In solid-state chemistry, the literature makes abundant use of terms such as “building blocks” or “secondary building units” (SBU), which are obviously a generalization of the retrosynthesis concept to 3D crystalline structures. However, one should be aware that speaking of a crystal structure using well-defined geometrical entities which reproduce the whole crystal structure using translation symmetry operators is not retrosynthesis. This is because we as yet have no experimental evidence for the existence of these objects as real chemical species. Consequently, in this paper we try to check that the retrosynthesis concept, so widely used in molecular or supramolecular chemistry, can be extended to solid-state chemistry. This means that we have to investigate how 1D, 2D or 3D networks may be the result of the association of some small, plausible chemical entities. In molecular or supramolecular chemistry this is straightforward, as strong covalent bonds and weak van der Waals or hydrogen bonds are easily identified using well-known atomic radii tables. It is this clear energetic discrimination which makes the identification of the building blocks so easy. A simple look at the very well known crystal structure of quartz shows bonds which look the same in every direction. This shuffles the cards in such an inextricable way that the validity of the building block concept becomes questionable. Retrosynthesis in solid-state inorganic chemistry is thus very often not possible ad oculos, and must then be computer-assisted.

This paper describes a very simple retrosynthetic tool based on the concept of atomic charge invariance upon extraction of a geometrical SBU (secondary building unit) from its crystalline environment. The first thing which must be known is the approximate atomic charge distribution in the crystalline network. Then, various building block units capable of generating, through translation, the whole network are sought (and at this stage one has complete freedom in doing this). Having a building block in hand, the same theoretical model is used to compute a new atomic charge distribution for this artificially isolated block. Now if $q_c(\mathrm{X})$ stands for the atomic charge borne by atom X in the crystal and $q_n(\mathrm{X})$ for its atomic charge in the extracted naked block, the ratio $\Delta q/q = 100 \times |q_c(\mathrm{X}) - q_n(\mathrm{X})|/q_c(\mathrm{X})$ should be a kind of Fukui function [14], allowing one to probe the susceptibility of an atomic site to its crystalline surrounding. If $q_c(\mathrm{X})$ cannot be changed, $q_n(\mathrm{X})$ can take any value as one is allowed to cut anywhere in the network. Consequently, $\Delta q/q$ ratios higher than 100% may occur, as they are just dimensionless susceptibility indexes and not true percentages (this would require some kind of normalization, which is missing in our definition). Our retrosynthetic postulate is that atoms showing a charge variation of a few per cent on going from the molecular to the solid state should be considered as corner-stones for the structure under investigation. Having identified some corner-stones, it is an easy matter to move along the pattern of chemical bonds, looking for a path connecting the greatest number of them. If such a path can be found, an aggregate of coordination polyhedra will emerge from the structure. If the structure of this particular block is understandable in terms of the basic chemical reactions of solid-state or solution chemistry, we believe that we can speak of a real chemical "tecton" [13], as it has emerged not from a purely geometrical analysis of the crystal but from a probing of its electronic density distribution. When no clear invariant path emerges from the structure, the tectons involved in the crystal growth process are most likely to be monomeric coordination polyhedra. Obviously, the choice of the theoretical model for obtaining the atomic charge distribution should be crucial. The key point is to use exactly the same model with the same parametrization for the crystal and the naked block, otherwise the charge differentials will be meaningless. Moreover, we also have to switch interactively and quickly from the molecular to the crystalline state. "Interactively" means the use of a high-performance graphical interface (the cheaper, the better), while "quickly" means that computing the whole charge distribution from the structure should be a matter of seconds and not of hours. These requirements have constrained us to develop our own GUI (graphical user interface) software, nicknamed WinPacha (acronym for Windows® partial atomic charges and hardnesses analysis). Technical details are given in Appendix A for interested readers. In the following we will systematically report the crystalline charge distribution q_i and the susceptibilty indexes $\Delta q/q(\%)$ associated with the extraction of an SBU from its crystalline environment. We will also report the partial electrostatic balances (PEB) computed from the charge distribution of the molecular or crystalline structure, as well as the ionicity index $I(\%)$ of the whole network. The PEB values allow us to judge the overall electrostatic stabilities of the structures investigated, while the ionicity index allows us to determine whether covalent ($I < 50\%$) or electrostatic ($I > 50\%$) bonds are the dominant interactions in a given crystal structure.

2. Elementary processes

Before performing our first computer-assisted retrosyntheses, we have to identify the basic chemical reactions involved when two coordination polyhedra share a corner, an edge or a face. For high-temperature solid-state syntheses, all reactions are basically charge neutralization between cations behaving as Lewis acids and anions behaving as Lewis bases. Increasing the temperature makes the coordination spheres of the cationic centers more flexible, allowing the direct exchange of oxo ligands between cationic centers. The situation is much more complex if the crystal has been grown from solution (sol–gel chemistry). From its very beginning, sol–gel chemistry has been divided into two main domains, according to the role played by water molecules in the process. If one chooses water as a solvent, then this is aqueous sol–gel chemistry. Water, with its ability to solvate both cationic species (through its lone pair localized on the oxygen atom) and anionic species (through its hydrogen-bond capabilities), is used in most industrial processes (coprecipitation techniques, hydrothermal synthesis, etc.) and also in many natural processes (weathering, crystal growth, biomineralization, etc.). Unfortunately, water is also a very good chemical reagent (through its derived ions H_3O^+ and OH^-), and a lot of chemical species are found in rapid equilibrium in a typical aqueous solution. For a long time, detailed structural characterization of these aqueous solutions was an impossible task. Nowadays, with the growing development of multinuclear NMR techniques, it is possible to study and follow the chemical transformations undergone by all the solute species. When water is not present in large amounts, it can only act as a chemical reagent, and this is organic sol–gel chemistry. This is the traditional domain of academic research, focussing on the elaboration of inorganic materials starting from metallo-organic molecular precursors.

2.1. Speciation

Speciation is concerned with the detailed structural characterization of stable species found in a solution or a melt of fixed composition under a given set of physicochemical conditions. For monomeric species, the speciation problem is solved when the coordination number and chemical composition of the first coordination sphere of metal cations is known. For oligomeric species, one must in addition know the number of coordination polyhedra per oligomer, and the connectivity pattern, i.e. how the vertices, edges or faces are shared between the constituent polyhedra. This problem can be solved by the simultaneous use of multinuclear nuclear magnetic resonance (NMR) spectroscopy, electron spin resonance (ESR) spectroscopy, infrared (IR) or Raman spectroscopies, ultraviolet or visible (UV–Vis) spectroscopy, extended X-ray absorption fine structure (EXAFS) or X-ray absorption near-edge structure (XANES) spectroscopies and Mössbauer spectroscopy. Among all these spectroscopic techniques, NMR is surely the most fruitful, as it gives access to both equilibrium and kinetic data. At this point, we have to stress that good knowledge of the dynamic properties of the various coordination polyhedra [15] is of the utmost importance before trying to tackle a chemical speciation problem. This comes from the fact that the definition of a coordination polyhedron is above all a matter of timescale. Some inorganic complexes are able to exchange their ligands at a quite considerable rate, rendering the building block concept completely meaningless, along with the definition of a coordination sphere! In other words, the longer the mean residence time of the ligands in the coordination sphere, the higher the probability that a given complex will behave as a chemically manipulable building block. Consequently, before embarking on retrosynthesis, one should be aware of the timescale of the underlying chemistry. This point has been over looked too often in the past, and fortunately NMR techniques are drastic remedies for this kind of amnesia.

2.2. *Hydrolysis*

This is the true starting point of sol–gel chemistry. In aqueous solutions, hydrolysis is a consequence of a change in pH, temperature, volume or ionic strength. If M stands for a metallic cation, hydrolysis leads to the appearance of M–OH bonds in solution:

$$\mathrm{M{-}OH_2^+ + H_2O \rightarrow M{-}OH + H_3O^+}$$

$$\mathrm{M{-}O^- + H_2O \rightarrow M{-}OH + OH^-}.$$

In non-aqueous solutions, hydrolysis is a consequence of adding water to reactive M–OR groups (where R is an organic group), ensuring the solubility of the complexes in an organic solvent (very often $R = C_nH_{2n+1}$, but any other organic radical may be used):

$$\mathrm{M{-}OR + H_2O \rightarrow M{-}OH + ROH}.$$

Very simple theoretical considerations can be used to explain the influence of pH on the $H_2O/OH/O$ ratios in the first coordination sphere of the ionic species, or the relative resistances of an organic groups towards hydrolysis [4,5]. The important point is to bear in mind the relative kinetics of these reactions. The first two are completely controlled by the diffusion of protons or hydroxide ions in the solution.

Consequently, they are to be placed among the fastest possible chemical reactions, with rate constants typically higher than $10^9\ s^{-1}$ [16]. In contrast, the last is basically a metal-based nucleophilic substitution, involving the addition of a water molecule and the breaking of both M–O and O–H bonds. Its kinetics will be driven mainly by the lability of the metal–oxygen bond, with rate constants ranging from $10^{-6}\ s^{-1}$ for the most inert M–O bonds up to $10^8\ s^{-1}$ for the most labile bonds [17].

2.3. Olation

This is the formation in solution of an hydroxo bridge between two cationic centers (M) with the elimination of a solvent molecule (S):

$$M{-}OH + M{-}S \rightarrow M{-}OH{-}M + S.$$

Very often, this condensation reaction follows an SN_1 mechanism, and the limiting step is thus the breaking of the M–S bond. In aqueous solutions ($S = H_2O$) the lability of the $M{-}OH_2$ bond is typically in the range 10^{-6}–$10^8\ s^{-1}$, depending mainly on the cationic charge z for main-group elements (the higher z is, the lower the lability), and on the electronic configuration for transition metals (depending on the crystal-field stabilization energy) [17]. With highly inert cations (Cr^{3+}, Co^{3+}) in aqueous solutions, it has been possible to show that olation is in fact a two-step process. First, a hydrogen bond is formed between the attacking OH group and the leaving water molecule, giving rise to a new hydrogen-bonded ligand $[H_3O_2]^-$ binding the two cationic centers [18]. This first weak bridge having been formed, nucleophilic substitution can now occur, leading to the formation of the much stronger M–OH–M bridge. Kinetic data concerning the olation reaction of multivalent metal cations have been reviewed elsewhere [19].

Virtually nothing is known about the occurrence of olation in non-aqueous solvents. This is probably due to the fact that hydroxo bridges are most easily formed and characterized when the cationic charge z is less than 3. With such a low z-value, metallo-organic precursors $M(OR)_z$ prefer to use OR bridges to reach their stable coordination state (typically $N=4$ or 6) rather than to add solvent molecules. With no solvent molecules in the first coordination sphere, olation cannot occur.

2.4. Oxolation

In this chemical reaction, an oxo bridge may be formed in solution between two cationic centers M after an elimination of a solvent molecule which was not initially present within the first coordination sphere of both partners:

$$M{-}OH + M{-}OR \rightarrow M{-}O{-}M + ROH.$$

As indicated, this kind of reaction occurs when the coordination sphere of the complexes are fully saturated with ligands having strong σ-donor capabilities. In aqueous solutions ($R = H$), there is just one possibility:

$$M{-}OH + M{-}OH \rightarrow M{-}O{-}M + H_2O,$$

whereas the above two reactions are in competition in non-aqueous solvents. Here the kinetics rely not only on the lability of the metal–oxygen bond, but also on the possibility of transferring a proton between the OH and OR groups. Referring to the general mechanism of proton transfer [16], this may occur following three different pathways:

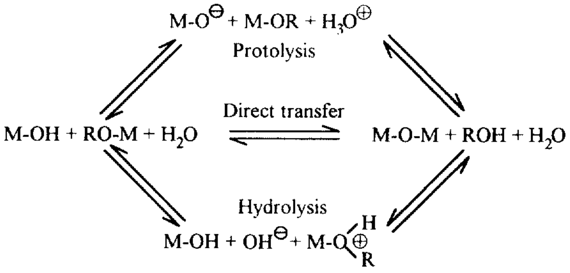

The oxolation kinetics is then strongly pH-dependent, as shown below in the case of the formation of the dichromate ion $[Cr_2O_7]^{2-}$ [20,21]:

$$[CrO_3(OH)]^- + [CrO_3(OH)]^- \rightleftharpoons [Cr_2O_7]^{2-} + H_2O \quad k_N \approx 2\ M^{-1}\ s^{-1},$$

$$[CrO_4]^{2-} + [CrO_3(OH)]^- \rightleftharpoons [Cr_2O_7]^{2-} + OH^- \quad k_B \approx 5 \times 10^{-4}\ M^{-1}\ s^{-1},$$

$$[CrO_3(OH)]^- + [CrO_2(OH)_2] \rightleftharpoons [Cr_2O_7]^{2-} + H_3O^+ \quad k_A \approx 2 \times 10^6\ M^{-1}\ s^{-1}.$$

This reaction is systematically rather slow, but can be activated by adding either H^+ ions (labilization of the M–OH or M–OR bond) or OH^- ions (deprotonation of the M–OH bond). Studies involving silicon alkoxides $Si(OR)_4$ have shown that elimination of a water molecule is slightly faster than elimination of an ROH molecule [22].

2.5. Heterocondensation

This reaction may occcur in solution when an hydroxo group is bonded to two different cationic centers, i.e. A–OH and B–OH:

$$A\text{–}OH + B\text{–}OH \rightarrow A\text{–}O\text{–}B + H_2O.$$

If $A = B = M$, this is just the oxolation reaction discussed above. If $A \neq B$, the two OH groups will have different acido-basic properties, one (A) favouring protolysis:

$$A\text{–}OH + H_2O \rightarrow A\text{–}O^- + H_3O^+,$$

and the other (B) favoring hydrolysis:

$$B\text{–}OH + H_2O \rightarrow B-OH_2^+ + OH^-.$$

The proton transfers being downhill in both cases, they no longer to the overall kinetics, and the formation of an oxo bridge is very easy:

$$A\text{–}O^- + B\text{–}OH_2^+ \rightarrow A\text{–}O\text{–}B + H_2O.$$

The kinetics should then be governed by the lability of the most basic complex, allowing the heterocondensation reaction to be as fast as the olation reaction of the cationic center B.

2.6. Secondary building units, tectons and structural building blocks

Using these five basic chemical reactions (speciation, hydrolysis, olation, oxolation and heterocondensation), a wide range of polynuclear and/or solid-state compounds (conveniently classified as 1D, 2D or 3D networks) may be synthetized. If high-temperature solid-state chemistry can use only the first reaction (speciation through acid–base neutralization), sol–gel syntheses have access to the whole palette. Playing with building blocks either in solution or in the melt is now theoretically possible, but a clear distinction should be made between real and hypothetical subunits. Starting from a given crystalline structure, it is generally very easy to identify secondary building units (SBUs) from which the target network may be reconstructed following strict geometrical rules (sharing of vertices, edges and/or faces). In the following, we will reserve the use of the term SBU to these hypothetical polyhedral subunits which allow a convenient description of the structure. Having some SBUs in hand, one may ask whether they provide real synthetic intermediates for the growth of a given crystalline phase. By submitting this SBU to our rational retrosynthesis tool, it can be transformed into a tecton (i.e. a chemical building block) which can be formed by known or presumed synthetic operations [13]. Here there is a basic difficulty in the recognition of a tecton as a definite chemical entity. If a given tecton is a real, active species responsible for the growth of a solid phase, its isolation and characterization should be extremely difficult. All that will be obtained is a mixture of mononuclear or polynuclear complexes (which are dead ends from which the active tecton can eventually be formed) in equilibrium with the infinite solid phase. This problem cannot be solved by chemistry, as it is rooted in the participation of translation symmetry operators to strong iono-covalent bonding. It may be that the SBUs resulting from the geometrical description of the crystal structure may just be an illusion resulting from some growth mechanism of other underlying hidden tectons. Making a clear distinction between tectons and SBUs should then be the first step towards the rational retrosynthesis of complex inorganic structures.

Our retrosynthetic approach has been developed in order to obtain a deeper understanding of the molecular processes involved in the syntheses of zeolites or other microporous solids. The description of these networks largely relies on the building block concept, despite the fact that the mechanisms of their formation remain relatively obscure. With very few exceptions, these solids are obtained under mild hydrothermal conditions using an aqueous medium to solubilize the starting compounds. Consequently, a good understanding of the chemistry involved in the formation of a microporous network cannot be reached without good knowledge

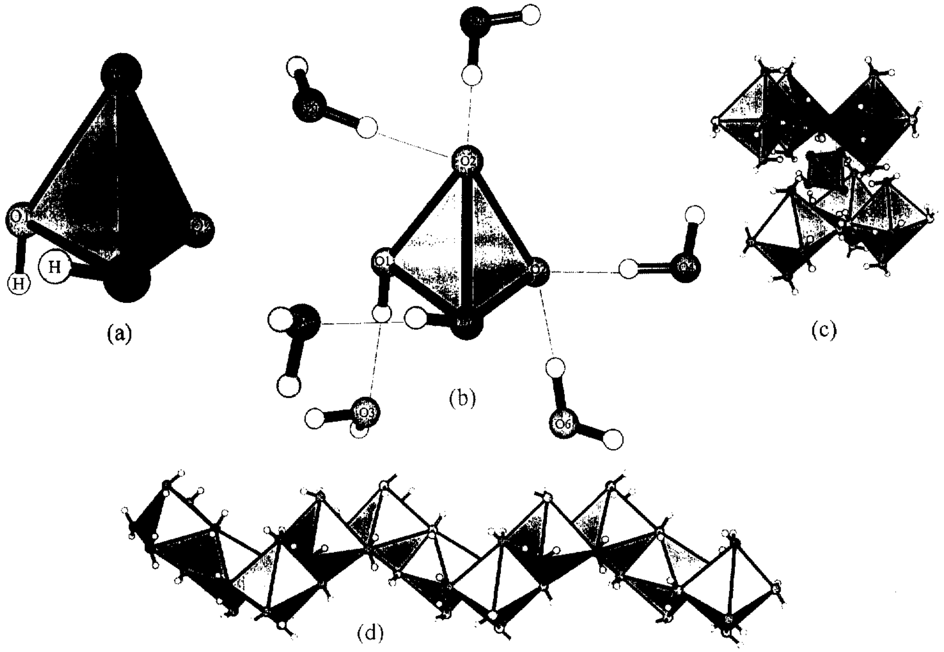

Fig. 1. Retrosynthesis of the crystal structure of $Na_2O.SiO_2.6H_2O$. (a) The naked $[SiO_2(OH)_2]^{2-}$ monomeric silicate anion. (b) Pattern of the hydrogen bonds in the hydrated $[SiO_2(OH)_2.6H_2O$ SBU. (c) Pattern of the hydrogen bonds in the mixed cationic $[Na_6(H_2O)_{32}][SiO_2(OH)_2]^{4+}$ SBU. (d) Topology of the linear infinite $[Na(H_2O)_4]^+$ octahedral chain.

of the ion–solvent interactions. From a structural point of view, corner-sharing between polyhedra seems to be the prerequisite for building a rather open network, whereas edge- or face-sharing favor the formation of dense, non-porous solids. This means that oxolation and not olation should be the main pathway to obtain a microporous phase, and that most building block candidates should be negatively charged species. Starting from a naked anion, three kind of interactions with the surronding medium are considered:

- hydrogen bonding with surrounding neutral solvent molecules, i.e. X–O···H–O–H;
- hydrogen bonding with solvated counter-cations, i.e. X–O···H–O–M; and
- electrostatic bonding with naked counter-cations, i.e. X–O···M.

The first kind of interaction should predominate under dilute conditions at low temperature, while the last should predominate at high temperature. The second interaction is of major importance in the field of hydrothermal synthesis, which uses moderate temperature conditions ($T < 300$ °C) and rather concentrated aqueous solutions. Moreover, it is known from ^{29}Si and ^{17}O NMR spectroscopies that the condensation reactions of SiO_4 tetrahedra are rather slow [23–27], demonstrating that the building block approach should be valuable. However, before studying the possible mechanisms of formation of microporous networks, it was thought that a validation of our retrosynthetic approach was needed on more simple silicate structures. We have thus limited this paper to the study of 0D (nesosilicates) and 1D (inosilicates) compounds, because it should be more easy to understand how an infinite linear chain of SiO_4 tetrahedra could emerge from the association of small molecular species rather than considering the formation of a fully 3D connected network.

3. Finite linear species

3.1. Silicate structures containing $[SiO_4]^{4-}$ monomers

The key point in understanding the growth mechanism of any silicated material is to get an idea of the relative magnitude of the three interactions outlined above. This can be reached by looking at the most simple building block unit, i.e. the isolated SiO_4 tetrahedron. In order to prevent condensation through oxolation, one must use strongly alkaline solutions. Under such conditions, the silicon atom is found as a di-protonated monomeric SiO_4 tetrahedron $[SiO_2(OH)_2]^{2-}$ [28]. From these solutions, it is possible to isolate the single-crystal phases $Na_2H_2SiO_4.nH_2O$, with $n=0$, 4, 5, 7 and 8. Let us have a look at the most hydrated phase ($n=8$), the crystal structure of which has been determined accurately on a fully deuterated phase using single-crystal neutron diffraction (space group Ibca, $\lambda=1.2640$ Å, $T=173$ K, $R=3.7\%$) [29]. Fig. 1(b) shows that we can extract from this network a $[SiO_2(OH)_2]^{2-}$ tetrahedron solvated by six water molecules. The two equivalent hydroxo groups (O1) are hydrogen-bonded to two water molecules (O3 at 276 pm and O4 at 277 pm). The two equivalent oxo groups (O2) are also hydrogen-bonded to two water molecules (O4 at 264 pm and O6 at 270 pm). These $[SiO_2(OH)_2]^{2-}.6H_2O$ solvates are further associated through additional hydrogen bonding in a sheet-like way, creating edge-sharing chains of octahedral sites occupied by sodium atoms [Fig. 1(d)]. Within each $[Na(H_2O)_6]^+$ octahedron, we find two di-μ_2-aquo bridges (atoms O5 and O6) and two terminal aquo ligands (O3 and O4) in the *cis* position with Na–O distances ranging from 242 to 249 pm.

If we look at the charges on oxygen atoms after the extraction of a naked $[SiO_2(OH)_2]^{2-}$ ion from the network [Fig. 1(a)], huge variations are observed (Table 1). This shows beyond any doubt that this naked ion cannot be considered as a tecton for the network. However, as soon as hydrogen bonding with water molecules is allowed, quite remarkable things happen. Upon extraction from the network of the solvated molecular species $[SiO_2(OH)_2]^{2-}.6H_2O$, oxygen atoms become strongly differentiated. Atoms O2, O3 and O4 are quite indifferent to the disappearance of the whole network (charge variations of less than 10%), whereas atoms O1 and O6 appear to be much more worried (O6 much more than O1). Consequently, an anisotropic $[SiO_2(OH)_2]^{2-}.6H_2O$ tecton can be easily defined in this structure. Its intrinsic anisotropy is revealed by the occurrence of $\infty[Na(H_2O)_4]^+$ linear octahedral chains [Fig. 1(d)], which surely would not exist without the periodic stacking of such entities. The chemical significance of this tecton

Table 1
Ionicity indexes, partial charges and charge variations according to molecular composition in $Na_2H_2SiO_4.8H_2O$

Index	% in $[SiO_2(OH)_2]^{2-}$	% in $[SiO_2(OH)_2]^{2-}.6H_2O$	Crystal
q(Si)	15	2	+0.67
q(O1)	94	16	−0.31
q(O2)	103	6	−0.32
q(O3)	–	6	−0.33
q(O4)	–	3	−0.35
q(O5)	–	–	−0.45
q(O6)	–	39	−0.46
q(H1)	130	20	+0.10
q(Na)	–	–	+1.02
I(%)	8.8	12.8	19.4
μ(D)	0.44	0.29	–
PEB (ev)	+1.0	−3.0	−25.0

is demonstrated by the fact that bringing close to it infinite linear chains of edge-sharing octahedra of monocharged sodium atoms has the main effect of changing the partial charge on atom O6, which is the only atom engaged in a μ_2-aquo bridge between two sodium atoms. This provides strong support for the idea that the molecular tectonics approach is a valuable one, provided that it is invoked by probing atomic susceptibility and not by just looking at the crystal structure from a very particular viewpoint which is highly dependent on the observer.

A look at the PEB of the isolated and solvated monomer shows the rather large decrease in energy (~4 eV) provided by authorizing hydrogen-bonding between the naked ion and the surrounding water molecules. A still more important decrease (~22 eV) comes from the association of the solvate with the singly charged sodium atoms. This decrease in energy would have been even more remarkable if the ionic species had not been solvated. For example, a typical naked $[SiO_4]^{4-}$ tetrahedron has a characteristic repulsive PEB value of +18 eV. By plunging this tetrahedron into a crystalline network of naked counter-cations, it is found that this PEB becomes −22 eV in Na_4SiO_4, −58 eV in olivines (e.g. forsterite Mg_2SiO_4), and −154 eV in garnets (e.g. pyrope $Mg_3Al_2(SiO_4)_3$) [30]. Moreover, the smaller the ionic radius, the stronger the electrostatic stabilization, as shown in the series M_2SiO_4 with M = Be (phenacite with PEB = −59 eV), Mg (forsterite with PEB = −58 eV), Ca (larnite with PEB = −50 eV), Sr (with PEB = −45 eV) and Ba (PEB = -35 eV) (Fig. 2).

In summary, these results show that the mere fact of writing anionic species on the paper immediately implies some interaction with the surrounding medium (neutral protic molecules or cationic entities) which should not be missed. As a rule of thumb, one can say that hydrogen bonding with solvent provides a stabilization energy of a few eV, hydrogen bonding to an hydrated counter-cation a few tens of eV, and direct interaction with a naked counter-cations a few hundreds of eV. With these orders of magnitude in mind, we can now consider more condensed crystal structures.

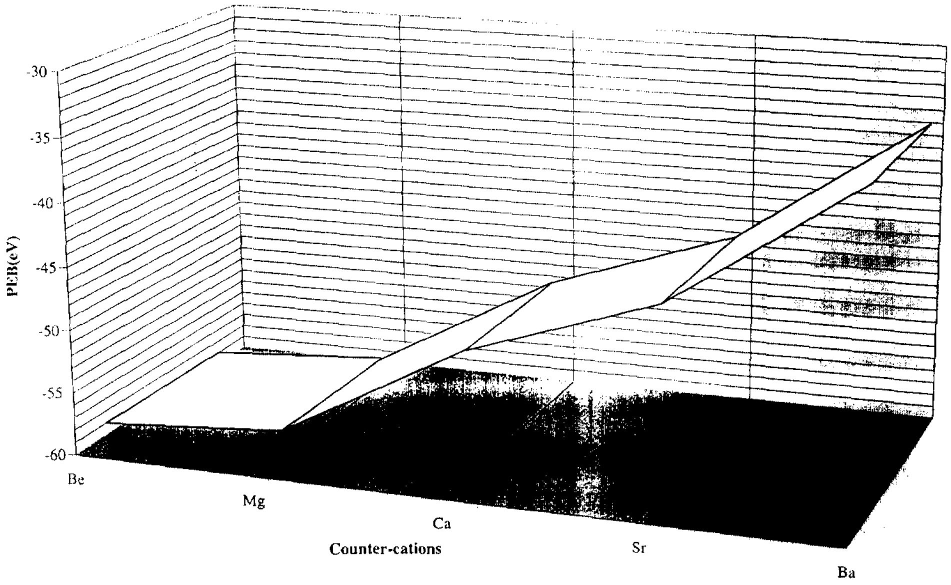

Fig. 2. Evolution of the partial electrostatic balance (PEB) of alkaline-earth orthosilicate M_2SiO_4 networks.

3.2. *Silicate structures containing pyrosilicate $[Si_2O_7]^{6-}$ dimers*

What can be said about the retrosynthesis of crystalline phases containing isolated corner-sharing dimers? At first sight, a pyrosilicate containing the $[Si_2O_7]^{6-}$ ion could be formed using two kinds of building blocks:

(1) a SiO_4 tetrahedron with all its charge-compensating shell which looks for a favorable crystalline site at which to react just here and nowhere else; and
(2) an already formed corner-sharing tetrahedral dimer which has only to lose its solvation shell to be incorporated at the right place in the crystal.

Is it possible to trace which pathway is the most likely to occur by looking at the final crystalline structure? The answer is surely yes. If the dimer is formed outside the crystal prior to its incorporation into the network, its basic feature (the existence of a bridging μ_2-oxo group) should be protected from interacting with the surrounding cations by the two silicon atoms. One can then expect that the partial charge borne by this bridging oxygen atom should not change very much (no more than a few per cent) on going from the naked state to the crystalline state. On the other hand, if the dimer is formed as a consequence of crystalline growth from monomeric species, all oxygen atoms would have been in interaction with the surrounding cations, and extracting the dimer from its crystalline state should have a more dramatic effect on the charge distribution.

Table 2 shows the results of calculations performed on 11 crystalline pyrosilicates displaying a wide range of Si–O–Si bond angles with a great variety of counter-

Table 2

Values of the PEBS, bond angles, partial charges with associated charge variations on the oxygen atom bridging two silicon atoms in 11 crystalline pyrosilicates. Note the rather constant value of the PEB of the naked $[\mathrm{Si_2O_7}]^{6-}$ ion, and the fact that the charge on the bridging oxygen atom either remains almost invariant upon extraction of the dimer from the network (upper part), or it undergoes a strong variation (lower part)

Crystal (space group)	$[\mathrm{Si_2O_7}]^{6-}$ PEB (eV)	Crystal PEB (eV)	θ(Si–O–Si) (°)	$q(\mu_2\text{-O})$
$\mathrm{Sc_2Si_2O_7}$ (C2/m) [31]	+45	−70	180	−0.66 (3%)
$\mathrm{Er_2Si_2O_7}$ ($\mathrm{P2_1/b}$) [32]	+47	−89	179	−0.68 (3%)
$\mathrm{Yb_2Si_2O_7}$ (C2) [33]	+44	−86	176	−0.68 (2%)
$\mathrm{Li_6Si_2O_7}$($\mathrm{P\bar{4}2_1m}$) [34]	+47	−66	136	−0.71 (3%)
$BaCuSi_2\mathrm{O_7}$ (Pnma) [35]	+47	−87	134	−0.71 (0%)
$\mathrm{Gd_2Si_2O_7}$ ($\mathrm{Pna2_1}$) [36]	+48	−81	159	−0.77 (20%)
δ-$\mathrm{Y_2Si_2O_7}$ (Pnam) [37]	+50	−70	157	−0.72 (18%)
$\mathrm{CaMgSi_2O_7}$($\mathrm{P\bar{4}2_1m}$) [38]	+45	−97	139	−0.82 (16%)
$Ca_3\mathrm{Si_2O_7}$ ($\mathrm{P2_1/a}$) [39]	+44	−91	136	−0.81 (10%)
$\mathrm{Sm_2Si_2O_7}$ ($\mathrm{P4_1}$) [40]	+45	−75	133	−0.66 (15%)
$\mathrm{BaBeSi_2O_7}$ (Pnma) [41]	+46	−74	129	−0.69 (9%)

cations. It is clear that despite the wide dispersion of space groups encountered, the partial charge on the bridging oxygen atom is either quasi-invariant on going from the molecular to the solid state (Sc, Er, Yb, Li, Ba–Cu) or undergo a change of at least 10% (Gd, Y, Ca–Mg, Sm, Ca, Ba–Be). It is then quite tempting to explain the existence of these two categories of crystal structures as a result of the occurrence of two completely different crystal growth mechanisms. We have shown previously that large cations provide less electrostatic stabilization than smaller cations. Incorporation of dimers which have less favorable PEB values should then be favored by small cations. This is completely verified in Table 2 for the $\mathrm{M_2Si_2O_7}$ phases if we arrange the cations according to their ionic size (Shannon and Prewitt values [42] averaged over the various coordination numbers in pm):

$$\mathrm{Li}(76)<\mathrm{Sc}(81)<\mathrm{Yb}(96)<\mathrm{Er}(98)<\mathrm{Y}(99)<\mathrm{Gd}(102)<\mathrm{Sm}(109)<\mathrm{Ca}(116).$$

For mixed phases $\mathrm{MM'Si_2O_7}$, one may infer that copper ($r_{\mathrm{ion}}=65$ pm) wins over barium ($r_{\mathrm{ion}}=147$ pm), whereas calcium or barium wins over magnesium ($r_{\mathrm{ion}}=71$ pm) and beryllium ($r_{\mathrm{ion}}=29$ pm), respectively. As can be seen from Table 2, there is no apparent correlation between the Si–O–Si bond angle value and the supposed growth mechanism. As shown in a previous study, this comes from the fact that electrostatic repulsions between unshared oxo groups prevent this angle becoming less than ~130° [30]. Above this critical value, the electrostatic contribution to the total Madelung energy is quite negligible, explaining the rather constant PEB value of the dimers extracted (46 ± 3 eV).

3.3. Silicate structures containing linear $[Si_3O_{10}]^{8-}$ trimers

The synthetic $Na_2Ca_3Si_3O_{10}$ phase (space group B2/b, PEB = −113 eV, I=42.5%) can be obtained through hydrothermal synthesis [43]. In this structure, three oxygens atoms have $\Delta q/q$ ratios of a few per cent [O4 = −0.91 (3%), O5 = −0.95 (4%) and O1 = −0.79 (5%)], other oxygen atoms being more affected [O2 = −1.03 (8%) and O3 = −0.97 (14%)]. A quick look at Fig. 3(a) shows that atoms O4 and O1 belong to the coordination polyhedron of atom Si1, forming the central core of the linear trimer. Atom O5, belonging to the two Si2 atoms defining the ends of the $[Si_3O_{10}]^{8-}$ trimer, a well-defined tecton of three corner-sharing tetrahedra, emerges from this structure.

This is not the case in the kilchoanite mineral phase $Ca_3Si_2O_7$ (space group I2 cm, PEB = −82 eV, I=43.3%) [44]. In this crystalline phase, best written as $Ca_6(SiO_4)(Si_3O_{10})$, the only oxygen atom having a low $\Delta q/q$ ratio is O7 with q= −0.90 (4%). As for other oxygen atoms belonging to the $[Si_3O_{10}]^{8-}$ trimeric SBU, q(O5) = −0.95 (10%), q(O8) = −0.92 (12%), q(O6) = −0.79 (17%) and q(O4) = −0.95 (18%). Atoms O1 (q = −0.99), O2 (q = −0.95) and O3 (q = −0.93) define an isolated $[SiO_4]^{4-}$ tetrahedra (Si1) coexisting with the linear trimer. Here it is clear that there is only one corner-stone belonging to the coordination sphere of atom Si2 situated at both ends of the trimer [Fig. 3(b)]. This rather dramatic role reversal relative to the $Na_2Ca_3Si_3O_{10}$ phase may well reflect a completely different growth mechanism, based on successive addition of monomeric SiO_4 tetrahedra acting as monodentate ligands (through atom O7) towards calcium atoms. The formation of the linear trimer should then be constrained by the overall $Ca_3Si_2O_7$ stoichiometry and space-group requirements. The presence of isolated SiO_4 tetrahedra in this structure brings strong support to the idea of a monomeric growth mechanism. This existence of two quite different crystal growth mechanisms may explain why the 3D conformations of both trimers are so different, with θ(Si2–Si1–Si2) = 164° in $Na_2Ca_3Si_3O_{10}$ (fully decaled Si1/Si2 conformer with PEB = +76 eV) and θ(Si2–Si3–Si2) = 98° in kilchoanite (fully decaled Si2/Si2 conformer with PEB = +82 eV).

The fully eclipsed Si2/Si3 conformer [Fig. 3(c)] is found in the rare mineral ardennite (space group Pnmm), which has the very complex structural formula [45]:

$$Mn_2(Mn,Ca)_2(AlOH)_4[(Mg,Al,Fe)OH]_2(As,V)O_4Si_3O_{10}(SiO_4)_2.$$

Since our software is not yet able to handle mixed crystal–solid solutions with different kinds of atoms occupying identical crystallographic sites, we cannot obtain the full crystalline charge distribution. However, extracting the trimer from the network remains possible, leading to PEB = +76 eV and $q(\mu_2\text{-O8}) = -0.74$. This last value is significantly different from the value found in $Na_2Ca_3Si_3O_{10}$ or kilchoanite (−0.79), suggesting the existence of a third growth mechanism which remains to be elucidated.

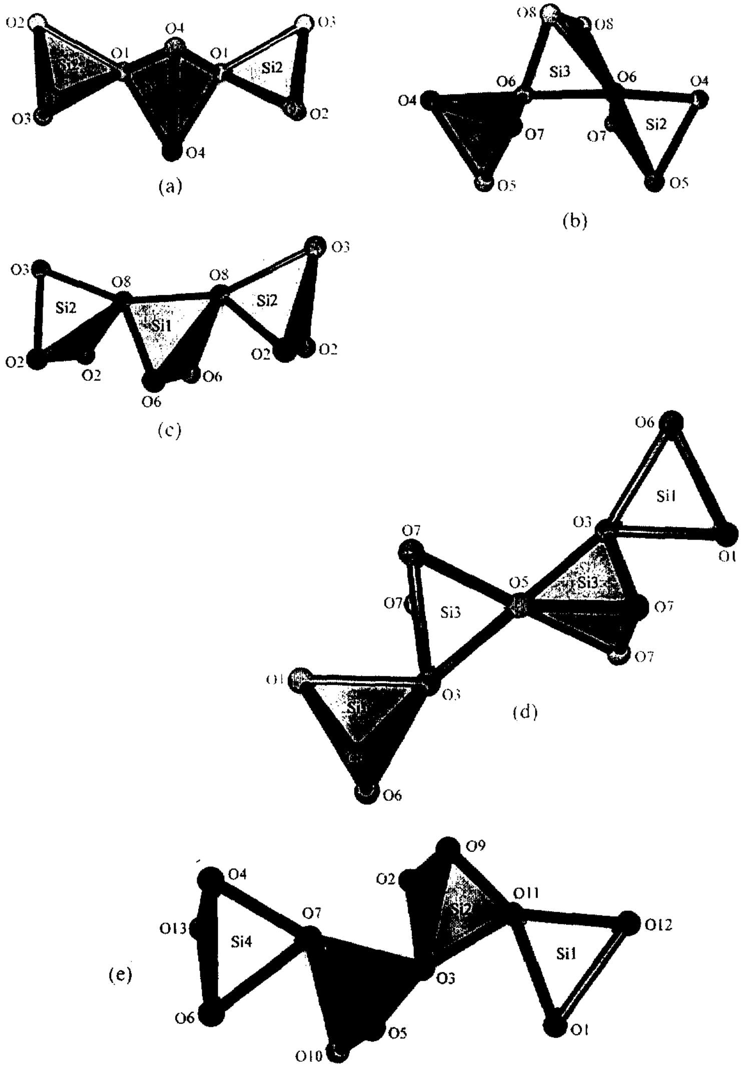

Fig. 3. Finite linear chain-like silicated polyanions. (a) Linear trimer in the synthetic $Na_2Ca_3Si_3O_{10}$ phase. (b) Linear trimer in kilchoanite $Ca_3Si_2O_7$. (c) Linear trimer in ardennite $Mn_2(Mn,Ca)_2(AlOH)_4[(Mg,Al,Fe)OH]_2(As,V)O_4Si_3O_{10}(SiO_4)_2$. (d) Linear tetramer in the synthetic $Ag_6Si_2O_7$ phase.(e) Linear tetramer in the synthetic $Ag_{10}Si_4O_{13}$ phase.

3.4. Silicate structures containing linear $[Si_4O_{13}]^{10-}$ tetramers

In the synthetic $Ag_{10}Si_4O_{13}$ phase (space group $P\bar{1}$ with PEB = −83 eV and I = 32.6%), a linear tetramer is found [Fig. 3(e)] displaying three non-equivalent μ_2-oxo groups with the following bond angle values [46]: θ(Si1–O11–Si2) = 147°,

θ(Si2–O3–Si3) = 138°, θ(Si3–O7–Si4) = 128°.The detailed crystalline charge distribution is given in Table 3, and shows that all oxygen atoms bonded to just one silicon atom display rather high $\Delta q/q$ ratios upon extraction of the linear tetramer (PEB = +110 eV), whereas those bridging two silicon atoms are much less affected. This susceptibility of "terminal" oxygen atoms to the removal of silver atoms and the lower ionicity found for this network in comparison with that of kilchoanite or $Na_2Ca_3Si_3O_{10}$ tends to prove that Ag^+ cations are not mere counter-cations in contrast with Na^+ or Ca^{2+}. In agreement, a wide dispersion of partial charges is found on the ten silver atoms, ranging from +0.59 up to +0.91. As regards the μ_2-oxo bridges it is also clear that oxygen O11 situated at one end of the tetramer is not very happy of the silver atoms kidnapping in deep contrast with its brother O7 placed at the other end. Taking atoms O7 and O3 as corner-stones, a linear trimeric tecton Si4–O7–Si3–O3–Si2 emerges from this structure, having undergone a condensation reaction with a Si1-based monomer. The association of two Si4–O7–Si3 and Si2–O11–Si1 tectonic dimers appears rather unlikely owing to the significant charge variation observed on atom O11.

Another kind of linear tetramer is found in the $Ag_6Si_2O_7$ phase, best formulated as $Ag_{18}(SiO_4)_2(Si_4O_{13})$ (space group C2/m, PEB = −46 eV, I = 33.6%) [47]. This tetramer displays two equivalent μ_2-oxo bridges with θ(Si1–O3–Si3) = 136° and one completely linear bridge with θ(Si3–O5–Si3) = 180° [Fig. 3(d)]. Here, the silver atoms do not appear to act as mere counter-cations (Table 4), ensuring a rather low ionicity in the crystalline network and a considerable spread of silver atomic charges, i.e. from +0.44 to +0.88. From a purely geometrical point of view, the tetramer conformation is most easily visualized as the association of two dimeric pyrosilicate SBUs with PEB = +105 eV. With virtually no charge differential on atom O3 and a significant variation on atom O5, the association of two Si1–O3–Si3 dimers through atom O5 is fully confirmed. The occurence of monomeric SiO_4 tetrahedra in this structure may be interpreted here as the signature of the failure to form a linear trimer before crystallization.

Is it possible to grow higher linear $[Si_nO_{3n+1}]^{2(n+1)-}$ oligomers through oxolation reactions in solution or through interaction with counter-cations in the solid state? Fig. 4 brings a definite answer by looking at the variation of the PEB of a linearly

Table 3
Partial charges on oxygen atoms in the synthetic phase $Ag_{10}Si_4O_{13}$ and $\Delta q/q$ ratios upon extraction of the linear tetramer $[Si_4O_{13}]^{10-}$ from the crystalline network. The mean partial charges on the non-oxygen atoms in the crystal are $\langle q(Ag)\rangle = +0.80 \pm 0.20$, $\langle q(SiQ^1)\rangle = +0.52 \pm 0.02$ and $\langle q(SiQ^2)\rangle = +0.61 \pm 0.05$

μ_5-O(SiAg$_4$)	μ_4-O(SiAg$_3$)	μ_3-O(SiAg$_2$)	μ_2-O(Si$_2$)
O1 = −0.84 (13%)	O8 = −0.85 (35%)	O12 = −0.82 (38%)	O3 = −0.67 (6%)
–	O4 = O13 = −0.84 (31%)	O9 = −0.81 (17%)	O11 = −0.66 (14%)
–	O10 = −0.84 (13%)	–	O7 = −0.63 (2%)
–	O6 = −0.82 (24%)	–	–
	O2 = −0.81 (17%)	–	–
	O5 = −0.80 (19%)	–	–
$\langle q\rangle = -0.84$	$\langle q\rangle = -0.83$	$\langle q\rangle = -0.82$	$\langle q\rangle = -0.65$

Table 4
Partial charges on oxygen atoms in the synthetic phase $Ag_6Si_2O_7$ and $\Delta q/q$ ratios (%) upon extraction of the linear tetramer $[Si_4O_{13}]^{10-}$ from the crystalline network. The mean partial charges on the non-oxygen atoms in the crystal are $\langle q(Ag)\rangle = +0.73 \pm 0.29$, $q(SiQ^0) = +0.46$, $\langle q(SiQ^1)\rangle = +0.51$ and $\langle q(SiQ^2)\rangle = +0.69$

μ_5-O(SiAg$_4$)	μ_4-O(SiAg$_3$)	μ_2-O(Si$_2$)
O2 = −0.86	O7 = −0.85 (13%)	O3 = −0.67 (2%)
–	O8 = −0.84	O5 = −0.66 (11%)
–	O4 = −0.82	
	O6 = −0.82 (35%)	
	O1 = −0.80 (28%)	
$\langle q\rangle = -0.86$	$\langle q\rangle = -0.83$	$\langle q\rangle -0.67$

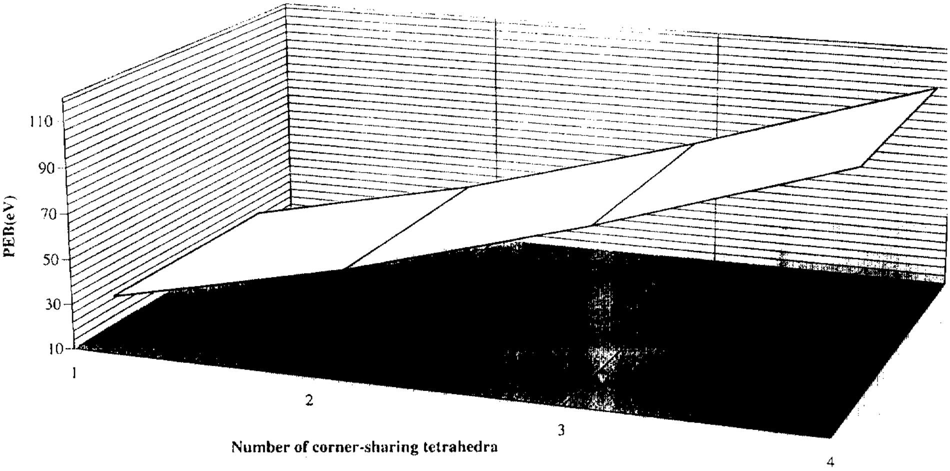

Fig. 4. Variation of the PEB of a linearly growing naked polysilicate $[Si_nO_{3n+1}]^{2(n+1)}$ chain as a function of the number of corner-sharing tetrahedra within the chain.

growing naked polysilicate chain,as a function of the number of tetrahedra n within the chain. Starting from PEB = +23 eV for an isolated $[SiO_4]^{4-}$ tetrahedron such as that found in olivines, values higher than +100 eV are obtained for $[Si_4O_{13}]^{10-}$ linear tetramers found in the synthetic silver silicates $Ag_6Si_2O_7$ or $Ag_{10}Si_4O_{13}$. As hydrogen bonding with solvated cations provides just a few tens of eV of stabilization, it is obvious from these data that linear growth in a solution of $[Si_nO_{3n+1}]^{2(n+1)-}$ species with $n > 4$ is rather unlikely. Accordingly, if a linear $[Si_4O_{13}]^{10-}$ tetramer is evidenced in aqueous silicate solutions through ^{29}Si NMR spectroscopy, this technique shows no evidence of the existence of longer chains [48,49]. Similarly, to the best of our knowledge no isolated $[Si_5O_{16}]^{12-}$ linear pentamer has yet been characterized in the solid state. This brings strong support to the high instability of linear $[Si_nO_{3n+1}]^{2(n+1)-}$ species with $n > 4$, either in solution or in the melt.

4. Silicate structures containing infinite $[SiO_3]^{2-}$ metasilicate chains

4.1. Alkaline-earth metasilicates:

We now investigate the retrosynthesis of an infinite linear chain of tetrahedra such as those found in the pyroxene family, i.e. $XYSi_2O_6$ (X, Y = Mg, Fe, Ca, etc.). In the light of the above discussion, the possible tectons should be limited to monomers, dimers or trimers. Accordingly, the linear chains found in the crystal structure of diopside $CaMgSi_2O_6$ and enstatite $MgSiO_3$ are best described with a reapeat unit based on two tetrahedra, whereas that of β-wollastonite $CaSiO_3$ contains three tetrahedra (Fig. 5). In diopside (C2/c, $Z=4$ [50]), a single tetrahedral chain is found with θ(Si–O3–Si) = 136°, leading to a network charge of q(O3) = −0.77, which displays a charge variation of 8% upon extraction of a $[Si_2O_7]^{6-}$ dimer. Two independent chains are found in enstatite. For the Pbca polymorph (orthoenstatite with $Z=16$) [51], the first chain is based on a bond angle of θ(Si1–O13–Si1) = 134°, leading to a network charge of q(O13) = −0.75, which changes by 3% upon extraction of a $[Si_2O_7]^{6-}$ dimer. The second chain, with a bond angle of θ(Si2–O23–Si2) = 128°, leads to q(O23) = −0.72 with a charge variation of 6%. For the $P2_1/c$ polymorph (clinoenstatite with $Z=8$ [52]), the first chain is based on a bond angle of θ(Si1–O3–Si1) = 133°, leading to a network charge of q(O3) = −0.75, which changes by 3% upon extraction of a $[Si_2O_7]^{6-}$ dimer. The second chain, with a bond angle of θ(Si2–O6–Si2) = 127° leads to q(O6) = −0.73 with a charge variation of 4%. Finally, the β-wollastonite phase is found as two polymorphs (triclinic $P\bar{1}$, $Z=6$ [53] and monoclinic $P2_1/a$, $Z=12$ [54]), which are both characterized by a single linear chain having three kinds of μ_2-oxo group. These two chains are only very slightly different, as in the triclinic phase we find: θ(Si1–O7–Si2) = 151°, θ(Si2–O8–Si3) = θ(Si1–O9–Si3) = 140°, q(O) = −0.72 (4%) and q(O8) = q(O9) = −0.73 (1%) PEB = −36 eV, to be compared with the monoclinic phase values θ(Si1–O9–Si2) = 150°, θ(Si2–O8–Si3) = 140°, θ(Si1–O7–Si3) = 139°, q(O9) = −0.71 (4%), q(O7) = -0.73 (1%) and q(O8) = −0.72 (1%) PEB = −35 eV.

Here, the $\Delta q/q$ ratios after extraction of a $[Si_2O_7]^{6-}$ dimer are found to be always less than 10%, but it is clear that the phase showing the highest $\Delta q/q$ ratio is diopside. Assuming that such a change of close to 10% is indicative of crystalline growth through the regular addition of monomers, much lower ratios should indicate growth involving oligomers. The occurrence of two kinds of linear metasilicate chain in orthoenstatite may then be the consequence of the coexistence of two independent growth mechanisms: one through dimers leading to the Si1–O5–Si1 chains ($\Delta q/q \approx 3\%$), and the other through monomers, leading to the Si2–O6–Si2 chain ($\Delta q/q \approx 6\%$). In clinoenstatite, both chains seems to involve dimers ($\Delta q/q = 3\%$ and 4%). In wollastonite, crystalline growth would involve trimeric tectons ($\Delta q/q \approx 1\%$ for bridging oxygen atoms belonging to atom Si3 against 4% for bridging atoms of belonging to atoms Si1 or Si2). Obviously, these subtle changes in growth mechanisms are monitored by the Ca/Mg ratio, which ranges from zero in enstatite up to infinity in wollastonite. Accordingly, oligomers seem to play an active role only if there exists in the surrounding medium a single kind of counter-cation (enstatite or

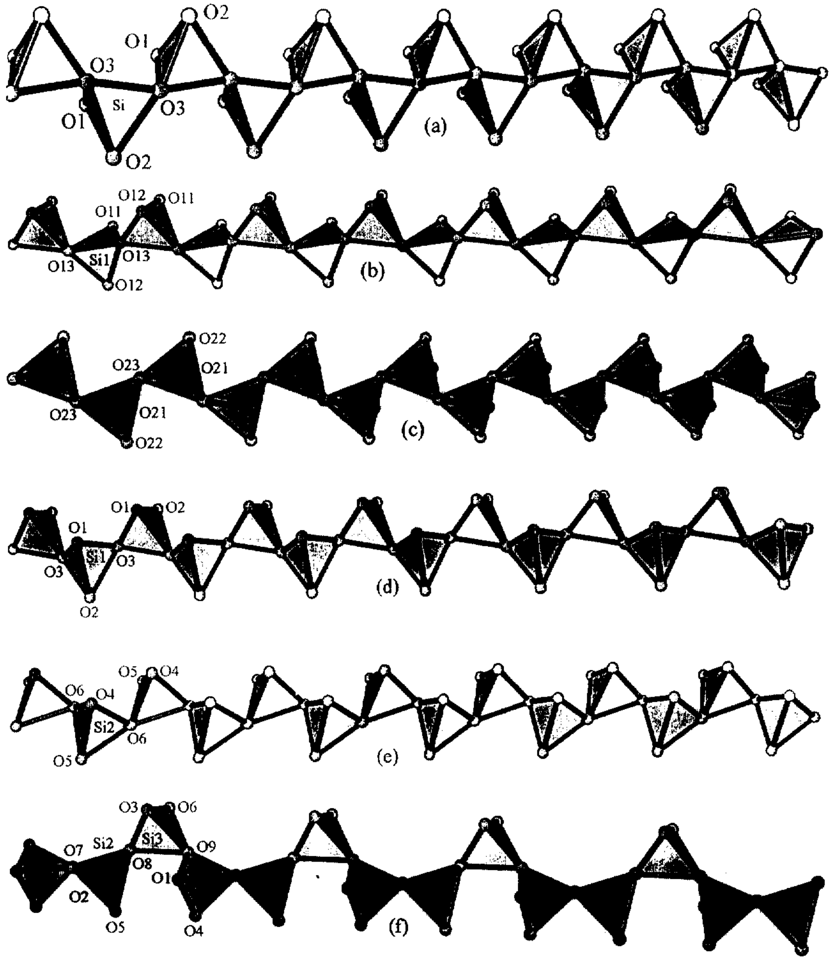

Fig. 5. Infinite linear chains of corner-sharing tetrahedra found in alkaline-earth metasilicates. (a) Chain in diopside $CaMgSi_2O_6$. (b) Chain based on atom Si1 in orthoenstatite $MgSiO_3$ (Pbca). (c) Chain based on atom Si2 in orthoenstatite $MgSiO_3$ (Pbca). (d) Chain based on atom Si1 in clinoenstatite MgSiOd3 ($P2_1/c$). (e) Chain based on atom Si2 in clinoenstatite $MgSiO_3$ ($P2_1/c$). (f) Chain in β-wollastonite $CaSiO_3$ ($P\bar{1}$). (g) Chain in parawollastonite $CaSiO_3$ ($P2_1/a$).

wollastonite). If some mixture occurs (diopside), monomeric growth becomes dominant.

4.2. Rhodonite $MnSiO_3$

The growth of alkaline-earth metasilicates can be explained by using three kinds of tectons: monomers $[SiO_4]^{4-}$ (diopside), dimers $[Si_2O_7]^{6-}$ (enstatite) or trimers $[Si_3O_{10}]^{8-}$ (wollastonite). More complex growth mechanisms seem to occur in the crystal structures of manganese metasilicates $MnSiO_3$, where linear chains of corner-sharing $[SiO_4]$ tetrahedra have also been evidenced. In rhodonite ($C\bar{1}$, $Z=20$ [55]), the chain can be described using a geometrical repeat unit based on five SiO_4 tetrahedra [Fig. 6(a)]. The chain of pyroxmangite ($C\bar{1}$, $Z=28$ [55]) has a repeat unit of seven corner-sharing tetrahedra [Fig. 7(a)]. Table 5 shows that it is virtually

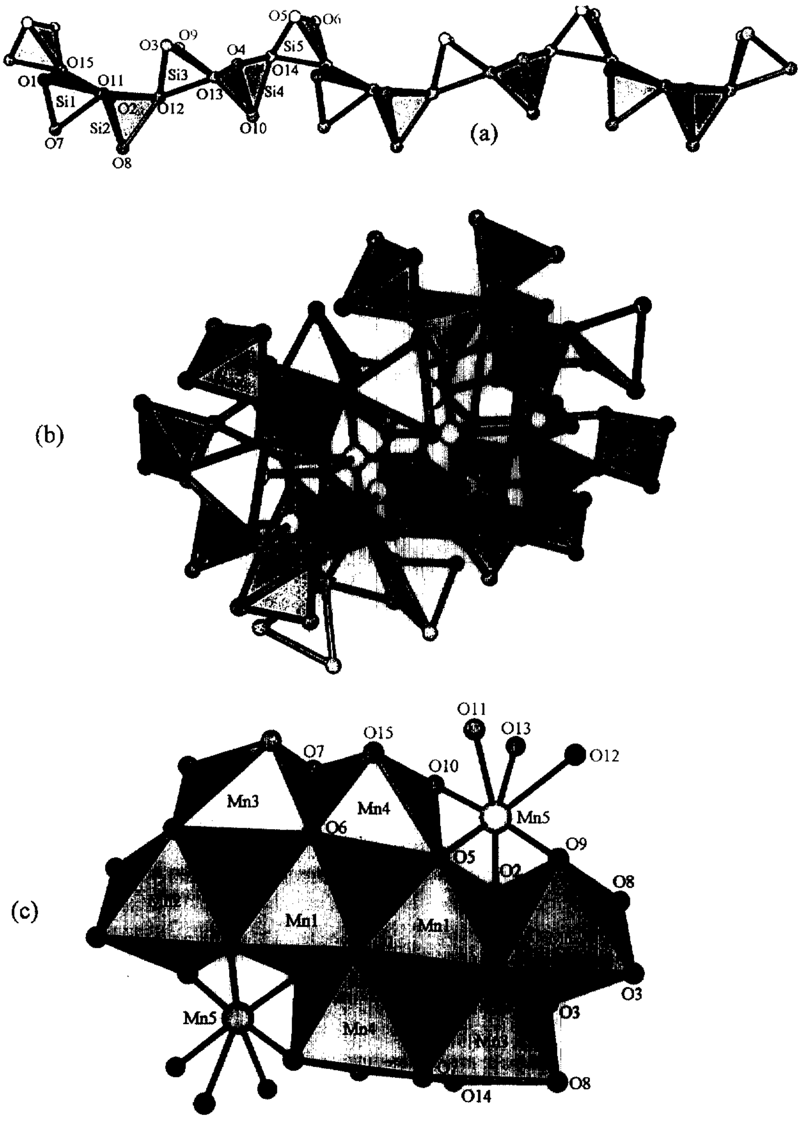

Fig. 6. Retrosynthesis of the crystal structure of rhodonite $MnSiO_3$ ($Z=20$). (a) Linear chain of corner-sharing tetrahedra. (b) Model cluster $[MnSi_3O_{10}]_{10}^{60-}$ extracted from the rhodonite network. (c) Manganese–oxygen core of the model cluster evidencing the pivot atom Mn5.

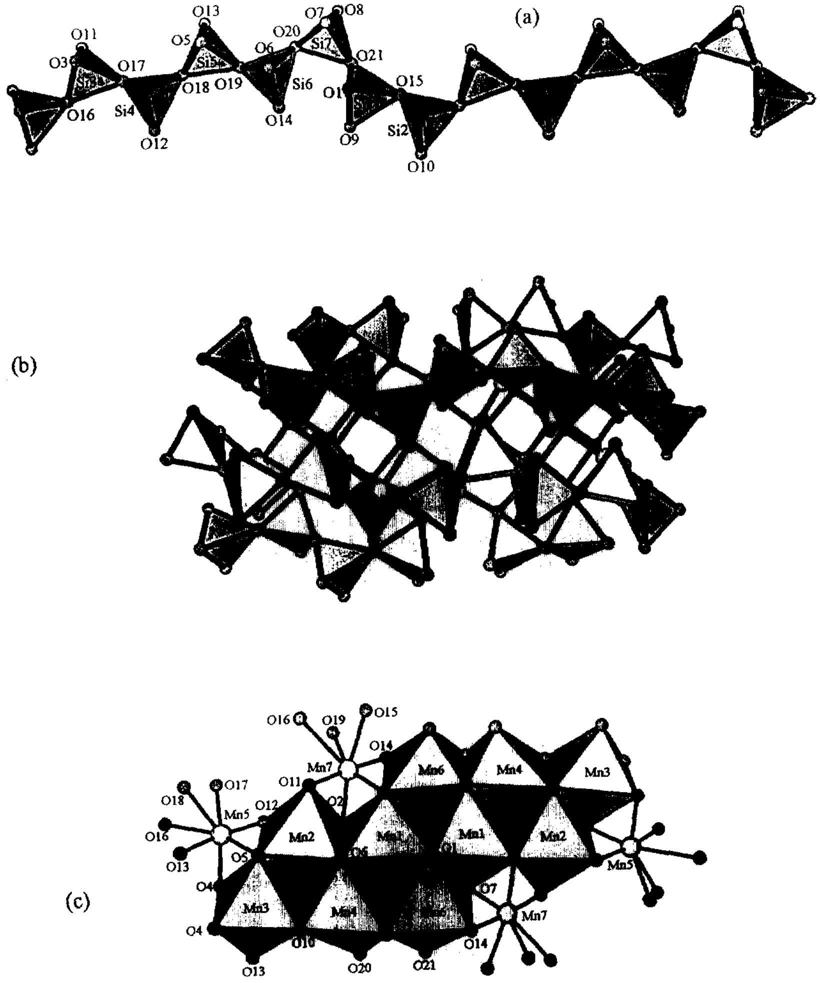

Fig. 7. Retrosynthesis of the crystal structure of pyroxmangite $MnSiO_3$ ($Z=28$). (a) Linear chain of corner-sharing tetrahedra. (b) Model cluster $[Mn_7Si_{21}O_{68}]_2^{76-}$ extracted from the pyroxmangite network. (c) Manganese–oxygen core of the model cluster evidencing the pivot atoms Mn5 and Mn7.

impossible to make a distinction between rhodonite and pyroxmangite in view of their relative charge distributions. However, these two phases are found to be of a very different nature to other metasilicates. Alkaline-earth metasilicates are virtually purely ionic compounds [$q(\mathrm{M})\approx 2$] with a very high charge gap between bridging and terminal oxo groups ($\Delta q > 0.2e^-$). In manganese metasilicates, the electronic density of the oxygen atoms is extensively transferred to the metal atoms, leading to a much more covalent network [$q(\mathrm{M})\approx 1$] and a smaller charge gap between bridging and terminal oxo groups ($\Delta q < 0.1e^-$). Obviously, this means that the condensation mechanism should be completely different in the two groups.

Table 5
Global ionicity indexes and averaged partial charges distributions in five pyroxene structures containing linear corner-sharing chains of SiO_4 tetrahedra

Metasilicate	Diopside	Enstatite	β-Wollastonite	Rhodonite	Pyroxmangite
Space group	C2/c	Pbca or ($P2_1/c$)	$P\bar{1}$ or($P2_1/a$)	$\bar{1}$	$\bar{1}$
PEB (eV)	−78.2	−43.5 (−43.8)	−35.9 (−35.3)	−14.5	−14.6
I (%)	44.0	46.2 (46.3)	42.4 (42.1)	26.7	26.8
$\langle\chi\rangle$ (eV)	2.36	2.86 (2.85)	1.79 (1.87)	5.75	5.75
$\langle\mu_4\text{-O(SiM}_3)\rangle$	−1.07	−1.14 (−1.15)	−1.01 (−1.00)	−0.60	−0.60
$\langle\mu_3\text{-O(SiM}_2)\rangle$	−0.91	−0.99 (−0.99)	−0.95 (−0.94)	−0.56	−0.56
$\langle\mu_3\text{-O(Si}_2\text{M)}\rangle$	−0.77	−0.74 (−0.75)	−0.73 (−0.72)	−0.53	−0.53
$\langle\mu_2\text{-O(Si}_2)\rangle$	–	–	–	−0.52	−0.52
⟨Si⟩	+0.78	+0.91 (+0.91)	+0.74 (+0.73)	+0.79	+0.79
⟨M⟩	+1.97	+1.96 (+1.96)	+1.96 (+1.95)	+0.89	+0.90

Accordingly, if we try to extract $[Si_2O_7]^{6-}$ dimers or $[Si_3O_{10}]^{8-}$ trimers from this structure, huge charge variations (~40%) are observed on the five μ_2-oxo groups (atoms O11–O15). This means that these bridging groups are not at all indifferent to the presence of manganese atoms, and that the condensation mechanism should involve both silicon and manganese atoms. The tectons responsible for the growth of this structure should then be manganese atoms strongly complexed by silicate species. Looking at the chain conformation of rhodonite [Fig. 6(a)], two retrosynthetic pathways could lead to the desired repeat unit: (1) complexation of Mn^{2+} cations by silicated dimers and monomers, and (2) complexation of Mn^{2+} cations by silicated linear trimers and dimers. From a purely statistical point of view, it seems obvious that the second pathway should be the correct one, as it involves the junction of two complexes instead of three for the first pathway. Nevertheless, can we reach the same conclusion from the charge differential ratios? The first thing we have do is to look in the network for a building block which is able to generate through translation not only the typical rhodonite metasilicate chain but also the strongly associated $\infty[MnO_3]^{4-}$ linear chain of edge-sharing MnO_6 octahedra. The following three-step sequence can be employed:

(1) generation of a $Mn_{10}O_{25}$ core after the exclusion of all silicon atoms;
(2) addition of silicon atoms with exclusion of all manganese and oxygen atoms; and
(3) addition of oxygen atoms with exclusion of all manganese and silicon atoms.

The cluster obtained using this sequence has $[MnSi_3O_{10}]_{10}^{60-}$ stoichiometry, and its geometry is displayed in Fig. 6(b). The reader can easily check that translating this 140-atom repeat unit along one direction would generate the rhodonite framework. Table 6, which gives the crystalline charge distribution and the $\Delta q/q$ ratios associated with the extraction of the $[Mn_{10}Si_{30}O_{100}]^{60-}$ cluster from the network, is very instructive. Seven oxygen atoms (O3, O5, O6, O9, O12, O14 and O15) have a $\Delta q/q$ ratio of less than 5%. Starting from these corner-stones, it is very easy to look for plausible tectons. For example, we can see that the four atoms O5, O6, O14 and O15 define the coordination polyhdron of atom Si5. With atom O14 making a bridge with atom Si4 ($\theta = 133°$) and atom O15 making a bridge with atom Si1 ($\theta =$

Table 6
Partial charges on oxygen atoms in rhodonite $[MnSiO_3]_5$ and $\Delta q/q$ ratios (%) upon extraction of a cluster $[MnSi_3O_{10}]_{10}^{60-}$ from the crystalline network. The mean partial charges on silicon and manganese atoms in the naked cluster are found to be $\langle q(Si)\rangle = +0.73 \pm 0.13$ and $\langle q(Mn)\rangle = +0.90 \pm 0.03$

μ_4-O($SiMn_3$)	μ_3-O($SiMn_2$)	μ_3-O(Si_2Mn)	μ_2-O(Si_2)
O1, O4 = −0.61 (5%)	O7 = −0.58 (10%)	O14 = −0.54 (0%)	O13 = −0.53 (28%)
O2 = −0.59 (5%)	O10 = −0.58 (5%)	O15 = −0.52 (2%)	O11 = −0.52 (25%)
O3 = −0.59 (3%)	O5 = −0.56 (0%)	–	O12 = −0.51 (2%)
O6 = −0.58 (0%)	O8 = −0.55 (11%)	–	–
–	O9 = −0.54 (2%)	–	–
$\langle q\rangle = -0.60$	$\langle q\rangle = -0.56$	$\langle q\rangle = -0.53$	$\langle q\rangle = -0.52$

136°), we obtain at least the trimer Si1–O15–Si5–O14–Si4. Now Si1 is linked to Si2 through atom O11 ($\theta = 130°$), and Si4 is linked to Si3 through atom O13 ($\theta = 146°$). With these last two atoms (O11 and O13) displaying strong charge variations, one can conclude with confidence that the first building unit should be the Si1–O15–Si5–O14–Si4 trimer acting as a multidentate ligand towards the atoms Mn1, Mn4 and Mn5. Turning our attention to the three remaining corner-stones, i.e. O3, O9 and O12, we are pleased to find that they all belong to the coordination sphere of atom Si3. With atom O12 making a bridge between atoms Si2 and Si3 ($\theta = 139°$), we obtain at least a Si2–O12–Si3 dimer, and cannot leave this dimer without avoiding the chain-breaking atoms atoms O11 and O13. From atom O3 we know that this dimer acts as a multidentate ligand towards the two remaining manganese atoms (Mn2 and Mn3), while from atom O9 we reach either atom Mn2 (dead end) or atom Mn5 belonging to the coordination sphere of a Si_3O_{10} building block. This allows us to select good tectonic candidates for the rhodonite network. If each silicate species is strongly associated with two manganese atoms (Mn2/Mn3 for the dimer and Mn1/Mn4 for the trimer), and if these two blocks are further associated via an uncomplexed Mn5 atom, we obtain one half of the cluster displayed in Fig. 6(b). This halved cluster, with a trimer on one side and a dimer on the other does not have symmetry required to iterate with the translation operators. Its dimerization through a center of inversion produces a fully symmetrical object (critical nucleus?) which can now be duplicated using translation symmetry operators [Fig. 6(c)]. Iterating in this way produces intimately interwoven MnO_3 and SiO_3 chains, one running (... Si3–Si2↔Si1–Si5–Si4↔Si3–Si2↔Si1–Si5–Si4 ...) in one direction and the other (... Si4–Si5–Si1↔Si2–Si3↔Si4–Si5–Si1↔Si2–Si3 ...) in the opposite direction (the arrow mean association through an uncomplexed Mn5 atom) [Fig. 6(b)].

4.3. Pyroxmangite $MnSiO_3$

Having a very appealing retrosynthetic pathway in hand for rhodonite, one can ask about the possibility of using a monomeric silicated manganese complex instead

of a dimeric complex. It is easy to show, following the procedure outlined above, that this would lead to the linear chain found in pyroxmangite [Fig. 7(a)]:
(1) generation of a $Mn_{14}O_{36}$ core after exclusion of all silicon atoms;
(2) addition of silicon atoms with exclusion of all manganese and oxygen atoms; and
(3) addition of oxygen atoms with exclusion of all manganese and silicon atoms.
This sequence, when applied to the pyroxmangite network, generates a 192-atom cluster having $[Mn_7Si_{21}O_{68}]_2^{76-}$ stoichiometry, which is shown in Fig. 7(b). Table 7 gives the crystalline charge distribution as well as its sensibility towards extraction of a $[Mn_7Si_{21}O_{68}]_2^{76-}$ block. The seven oxygen atoms bridging two silicon atoms can be clearly divided into two groups: O15, O16 and O19, which display $\Delta q/q$ ratios higher than 10%; and O17, O18, O20 and O21, which display $\Delta q/q$ ratios lower than 10%. For atoms O17 and O18, belonging to the coordination sphere of atom Si4, and atoms O20 and O21, belonging to the coordination sphere of atom Si7, two trimeric units may be identified: O19–Si5–O18–Si4–O17–Si3–O16 and O19–Si6–O20–Si7–O21–Si1–O15. In this last trimer, atom Si7 has a clear core role as it displays four quasi-invariant oxygen atoms (O7, O8, O20 and O21). Next in order comes atom Si6, which has two quasi-invariant atoms (O6 and O20), and last Si1 with just O21. This trimer is then found to behave as a tridentate ligand towards atom Mn1 through atoms O6, O7 and O8 and as a monodentate ligand towards atom Mn6 through atom O8. In the first trimer, atoms Si4 and Si3 both display three quasi-invariant oxygen atoms (O12, O17 and O18, and O3, O11 and O17 for Si4 and Si3, respectively), while atom Si5 has just one O18. This trimer is also found to behave as a tridentate ligand towards atom Mn2 through atoms O3, O11 and O12 and as a tridentate capping ligand towards atom Mn5 through atoms O12, O17 and O18. Now only atom O10 remains, with a $\Delta q/q$ ratio of less than 5%, which belongs to the coordination shell of atoms Si2 and acts as a bridging ligand between atoms Mn3 and Mn4. The only as yet unvisited metallic center is atom Mn7, which can be reached from both trimeric species (through atom O7 or O11).

Consequently, both structures (rhodonite and pyroxmangite) can be described as the heterocondensation of silicated complexes of the Mn^{2+} ion. In rhodonite, the pivot atom seems to be Mn5 monitoring the association of $Mn_2Si_2O_7$ and

Table 7
Partial charges on oxygen atoms in pyroxmangite $[MnSiO_3]_7$ and $\Delta q/q$ ratios (%) upon extraction of a $[Mn_7Si_{21}O_{68}]_2^{76-}$ cluster from the crystalline network. The mean partial charges on silicon and manganese atoms in the naked cluster are found to be $\langle q(Si) \rangle = +0.71 \pm 0.14$ and $\langle q(Mn) \rangle = +0.92 \pm 0.05$

μ_4-O($SiMn_3$)	μ_3-O($SiMn_2$)	μ_3-O(Si_2Mn)	μ_2-O(Si_2)
O6 = −0.62 (3%)	O14 = −0.59 (5%)	O20 = −0.54 (6%)	O18 = −0.53 (0%)
O1, O5 = −0.61 (5%)	O9 = −0.58 (10%)	O21 = −0.52 (4%)	O19 = −0.53 (17%)
O2 = −0.60 (5%)	O7 = −0.56 (0%)	–	O15 = −0.52 (19%)
O4 = −0.60 (7%)	O10, O12 = −0.56 (3%)	–	O16 = −0.52 (33%)
O3 = −0.59 (3%)	O11 = −0.55 (3%)	–	O17 = −0.52 (2%)
O8 = −0.58 (0%)	O13 = −0.55 (16%)	–	–
$\langle q \rangle = -0.60$	$\langle q \rangle = -0.56$	$\langle q \rangle = -0.53$	$\langle q \rangle = -0.52$

$Mn_2Si_3O_{10}$ species. In pyroxmangite, the pivot center is atom Mn7 which monitors the association of Mn_2SiO_4 monomers with two kinds of $Mn_3Si_3O_{10}$ trimer. In both cases, the formation of the corner-sharing $\infty[SiO_3]^{2-}$ tetrahedral chain cannot be decorrelated from the formation of a more complex $\infty[MnO_3]^{4-}$ edge-sharing octahedral chain, in a way which is strongly reminiscent of a molecular recognition process.

4.4. *Alkali antimony(V) silicate $CsSbO(SiO_3)_2$*

Quite recently, Pagnoux et al. [56] obtained a new kind of $\infty[SiO_3]^{2-}$ chain silicate by reacting a mixture of $CsNO_3$, Sb_2O_3 and SiO_2 in a 2:1:2 molar ratio. This phase, with $CsSbO(SiO_3)_2$ stoichiometry (space group Pna2$_1$, PEB = −43 eV, I = 28.5%), is found to have a global ionicity which is very similar to that of $MnSiO_3$ frameworks. However, the presence of Cs atoms explains its much lower mean electronegativity ($\langle\chi\rangle = 4.93$ eV) and PEB. Fig. 8(a) shows the conformation of the infinite chain, which seems to be easily reproduced using three $[Si_2O_7]$ SBUs. As with the $MnSiO_3$ phases, the extraction of dimers from this network leads to charge variations on oxygen atoms bridging two silicon atoms of at least 40%, denying them any tectonic role. Table 8 give the crystalline charge distribution of this network, whose retrosynthesis was performed as follows:

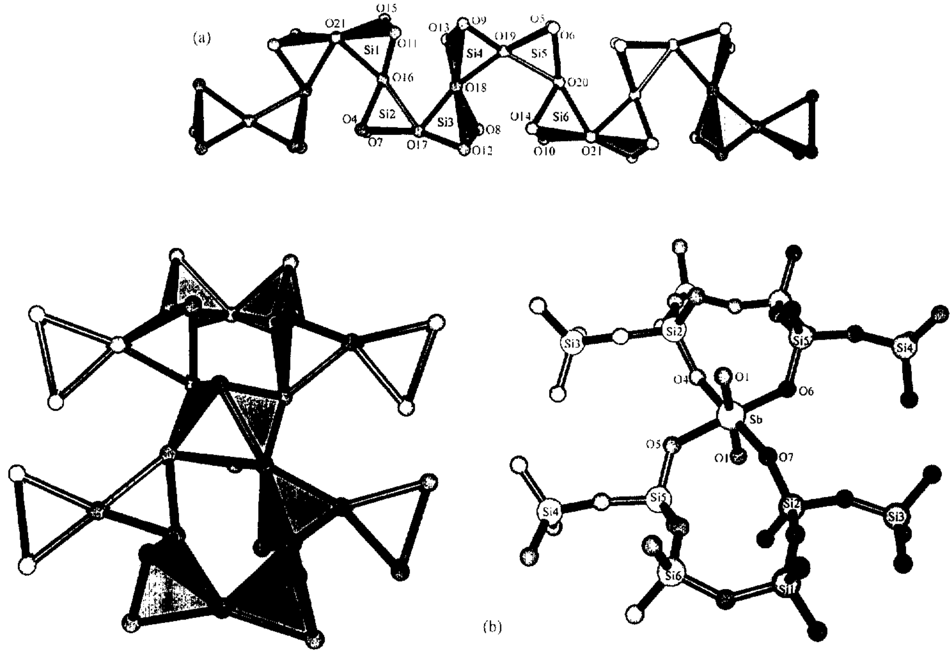

Fig. 8. Retrosynthesis of the crystal structure of an alkali antimony(V) silicate $CsSbO(SiO_3)_2$. (a) Chain of corner-sharing SiO_4 tetrahedra. (b) Model cluster $[SbSi_{12}O_{40}]^{27-}$ extracted from the network.

Table 8
Crystalline partial charges on oxygen atoms in the synthetic silicate $CsSbO(SiO_3)_2$. The mean partial charges on silicon, antimony and caesium atoms are found to be $\langle q(Si)\rangle = +0.84 \pm 0.05$, $\langle q(Sb)\rangle = +1.58 \pm 0.01$ and $\langle q(Cs)\rangle = +1.00$

μ_2-O(Sb$_2$)	μ_3-O(SiSbCs)	μ_2-O(SiSb)	μ_2-O(Si$_2$)
O3 = −0.68	O12 = −0.64	O9 = −0.64	O17 = −0.57
O1 = −0.67	–	O5, O7, O8, O10 = −0.63	O19 = −0.56
O2 = −0.66	–	O6, O15 = −0.62	O18, O21 = −0.55
–	–	O4, O13 = −0.61	O20 = −0.53
–	–	O11, O14 = −0.60	O16 = −0.52
$\langle q\rangle = -0.67$	$\langle q\rangle = -0.64$	$\langle q\rangle = -0.62$	$\langle q\rangle = -0.55$

(1) generation of an SbO_6 octahedron masking all caesium and silicon atoms;
(2) addition of silicon atoms masking all caesium, antimony and oxygen atoms;
(3) addition of oxygen atoms masking all caesium, antimony and silicon atoms;
(4) addition of silicon atoms masking all caesium, antimony and oxygen atoms; and
(5) addition of oxygen atoms masking all caesium, antimony and silicon atoms.

The resulting cluster, with $[SbSi_{12}O_{40}]^{27-}$ stoichiometry, is displayed in Fig. 8(b). For this cluster, we find $\langle q(Sb)\rangle = +1.60$ and $\langle q(Si)\rangle = +0.67$ with charge invariance ($\Delta q/q$ ratios less than 5%) on just four atoms: O4 (2%), O5 (2%), O6 (2%) and O7 (3%). All these atoms make a bridge between the Sb1 atom and a silicon atom belonging to a crankshaft silicate chain, and the growth mechanism is supposed to be a heterocondensation between antimony atoms and monodentate SiO_4 tetrahedra. Applying to this critical nucleus the symmetry translation operators along the *c*-axis generates corner-sharing chains of silicated SbO_6 octahedra, while applying these operators in the *a*,*b*-plane forces the formation Si–O–Si bridges to maintain electroneutrality. As expected, the presence of caesium atoms is necessary to provide the necessary reticular energy, but they seem to play no role by themselves in the self-assembly of the covalent framework.

4.5. Double silicate chain in amphiboles

To conclude this study of inosilicate structures, we wish to investigate the double silicate chain characteristic of amphibole minerals [Fig. 9(a)]. Amphiboles are important rock-forming minerals having the general formula $X_{2-3}Y_5Z_8O_{22}(OH,F)_2$, where X and Y stand for metallic cations having an ionic radius higher than 66 pm and lower than 80 pm, respectively, and Z is Si, Al or Fe^{3+}. Table 9 gives the partial charge distribution computed for a fully stoichiometric fluortremolite $Ca_2Mg_5Si_8O_{22}F_2$ [57]. From a purely structural point of view, the amphibole double chain $\infty[Si_4O_{11}]^{10-}$ can be derived from the condensation side-by-side of two pyroxenoid $\infty[SiO_3]^{2-}$ linear chains, similar to that found in diopside or enstatite. Knowing that the diopside chain should grow through the association of Ca^{2+} or Mg^{2+} cations with $[SiO_4]^{4-}$ monomers, the same growth mechanism may be anticipated for the tremolite phase. Accordingly, we have been unable to find in this structure

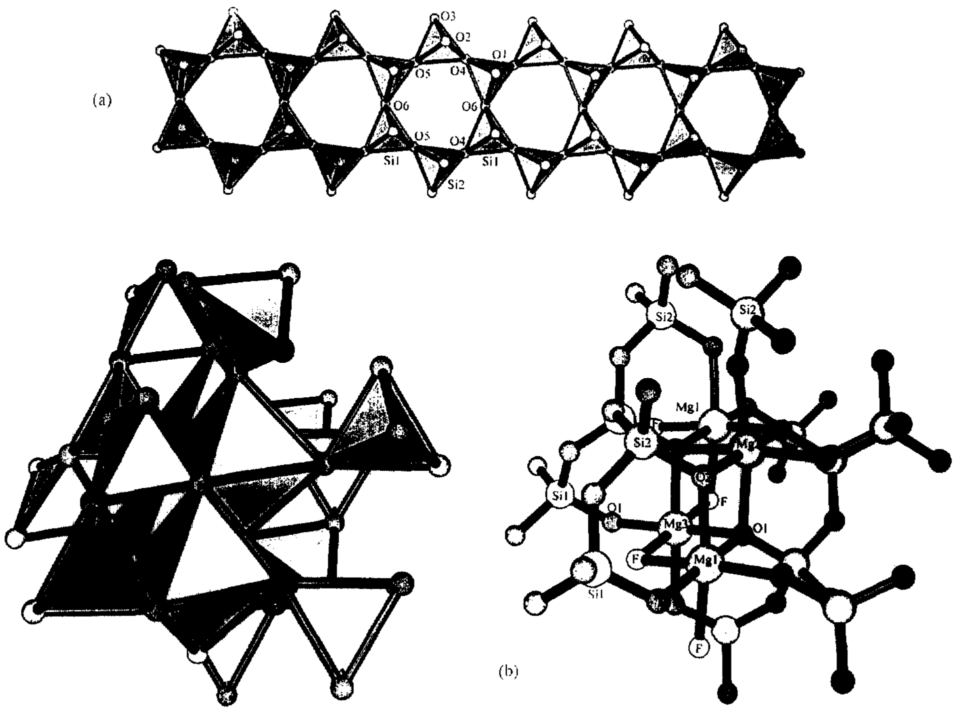

Fig. 9. Retrosynthesis of the crystal structure of a fluortremolite. (a) The double chain of corner-sharing tetrahedra characteristic of the amphibole structure. (b) Model $[MgSi_3O_{10}F]_4^{28-}$ cluster extracted from the network.

Table 9
Crystalline partial charge distribution in a fluortremolite phase $Ca_2Mg_5Si_8O_{22}F_2$. The global ionicity indexes of this phase are found to be PEB = −242 eV, $I = -39.3\%$ and $\langle\chi\rangle = 4.12$ eV

Crystalline site	Atomic partial charge
μ_3-F(Mg_3)	F1 = −1.00
μ_4-O($SiMg_3$)	O1 = −0.97
μ_4-O($SiMg_2Ca$)	O2 = −0.96
μ_3-O(SiMgCa)	O3 = −0.84
μ_3-O(Si_2Ca)	O5 = −0.61, O4 = −0.58
μ_2-O(Si_2)	O6 = −0.45
SiO_4	Si2 = +0.79, Si1 = +0.83
MgO_6	Mg2 = +1.50
MgO_4F_2	Mg1 = +1.76, Mg3 = +1.85
CaO_8	Ca1 = +1.93

any invariant partial charge by looking at naked dimers or trimers. Trying to generate a magnesium-based model cluster is here of no help. The following sequence: (1) generation of a $Mg_4O_{12}F_4$ core masking all calcium and silicon atoms;

(2) addition of silicon atoms masking all calcium and magnesium atoms; and
(3) addition of oxygen and fluorine atoms masking all calcium, silicon and magnesium atoms

leads to a 60-atom model cluster with $[MgSi_3O_{10}F]_4^{28-}$ stoichiometry, as displayed in Fig. 9(b). After computation, it is found that only two atoms show charge invariance relative to the full network, namely O1 ($\Delta q/q = 1\%$) and F ($\Delta q/q = 1\%$). This is a rather meager harvest for a self-evident silicate double-chain. Approximate charge invariance may, however, be found (but with no discrimination between atomic sites) only after generation of a spherical cluster having a radius of ~6 Å. This absence of obvious tectons in this structure may be the key to understanding the extreme variability in chemical composition of natural amphiboles. This brings strong support to the idea that the growth mechanism of such a phase should involve only SiO_4 monomers associated with a wide range of rather indifferent counter-cations. Consequently, the growth mechanism of $\infty[Si_4O_{11}]^{10-}$ linear double chain of amphiboles remains a well-kept secret. It is also possible that the occurrence of this chain is just an illusion resulting from the application of symmetry translation operators to an assembly of MO_8, MO_6 and TO_4 monomeric polyhedral units.

5. Silicate structures containing insular $[SiO_3]_n^{2-}$ rings

The above discussion has shown that even the nucleation and growth of a linear, infinite silicate chain can be analyzed with very few tectonic units, such as monomers, dimers and trimers. The reason for this is rooted in Fig. 4, which shows the steep increase in repulsive energy associated with the successive addition of naked tetrahedra in a purely linear fashion. The formation of a linear chain becomes possible only when at some stage of the growth process, a counter-cation is associated with the $[SiO_4]^{4-}$ tetrahedra. If there are not enough counter-cations for each of the terminal oxygen atoms of a SiO_4 tetrahedron, the linear chain will never be formed. In such a case, the formation of a ring is most likely to occur. The problem which remains to be solved is the possible tectonic role of such rings in the growth of a 3D silicated network. We will show in the following that silicate rings are also limited in size by the accumulation of negative charges on terminal oxygen atoms. However, because they have less terminal atoms than linear silicated chains, a greater number of SiO_4 tetrahedra may be involved in ring formation.

5.1. *Silicate structures containing the $[Si_3O_9]^{6-}$ ring*

A quite remarkable situation is encountered in pseudo-wollastonite α-$CaSiO_3$ (space group $C\bar{1}$, $Z = 24$, PEB = −33 eV, $I = 40.7\%$) [58]. The charge distribution in this network is found to be $q(Ca) = +1.94 \pm 0.05$, $q(Si) = +0.64 \pm 0.01$, $q[\mu_4\text{-}O(SiCa_3)] = -0.91 \pm 0.02$ and $q[\mu_4\text{-}O(Si_2Ca_2)] = -0.76 \pm 0.01$. Upon extraction of the two non-equivalent $[Si_3O_9]^{6-}$ rings (PEB = +37 and +39 eV) from this network [Fig. 10(a)], it is found that $\Delta q/q < 3\%$ for the 12 unshared corners (atoms O1–O12) against $\Delta q/q = 13\%$ for the six shared corners (atoms O13–O18). The only

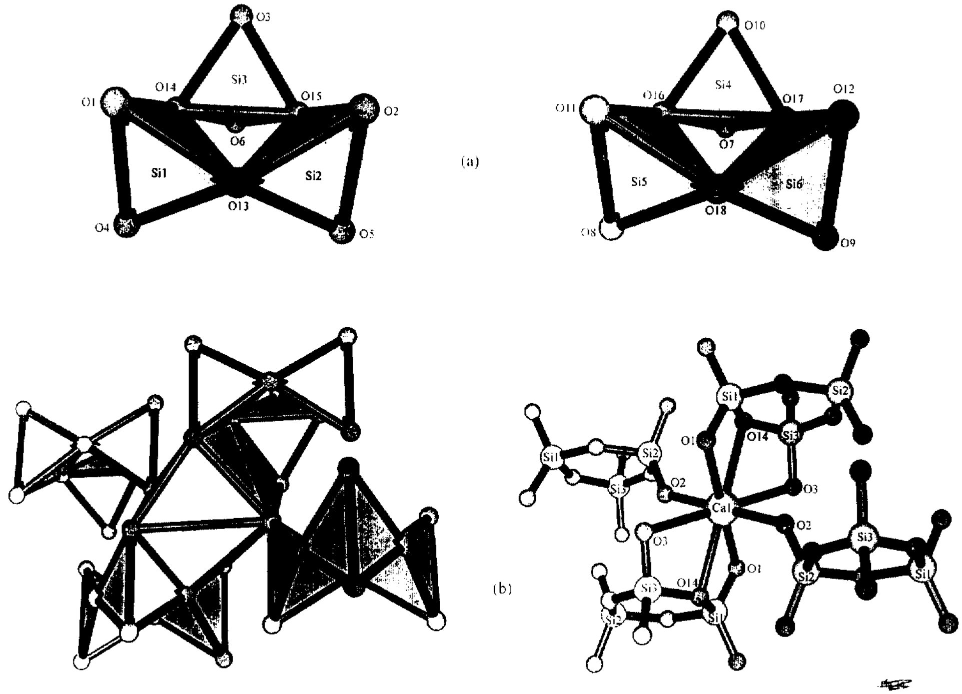

Fig. 10. Retrosynthesis of the crystal structure of pseudo-wollastonite α-$CaSiO_3$. (a) The two trimeric Si_3O_9 rings of corner-sharing SiO_4 tetrahedra. (b) Model cluster $[Ca(Si_3O_9)_4]_{12}$ extracted from the network with an eight-fold coordinated calcium atom with both bidentate and tridentate coordination modes for the Si_3O_9 rings.

way to explain the charge invariance observed simultaneously on all unshared corners is to suppose that the $[Si_3O_9]^{6-}$ ring is a real tecton for this structure, with shared corners behaving as ligands towards calcium atoms. This participation of shared oxygen atoms in the coordination sphere of calcium atoms is evidenced in Fig. 10(b). Each eight-fold coordinated calcium atom is found to be surrounded by four $[Si_3O_9]^{6-}$ rings, with two rings acting as monodentate ligands (shortest Ca–OSi bonds of 230 ± 2 pm) and the two others as tridentate ligands (longest Ca–O distances of 259 ± 2 pm for one Ca–OSi or Ca–OSi_2 bond and 267 ± 3 pm for the other Ca–OSi bond). This pseudo-wollastonite structure thus clearly shows that ring formation may lead to charge invariance on unshared corners rather than on shared corners. This result is obviously a consequence of the much greater rigidity of a ring. In contrast, the flexibility of chain-like species confers a much greater sensitivity of the unshared corners to the crystalline environment, limiting the charge invariance to shared corners.

Another kind of $[Si_3O_9]^{6-}$ ring [Fig. 11(a)] is found is the structure of benitoite $BaTiSi_3O_9$ (space group $P\bar{6}c2$, $Z = 2$, PEB $= -68$ eV, $I = 32\%$) [59]. The crystalline charge distribution is found to be $q(Ba) = +2.02$, $q(Ti) = +1.50$, $q(Si) = +0.84$, $q[\mu_2\text{-O1}(Si_2)] = -0.61$ and $q[\mu_2\text{-O2}(SiTi)] = -0.70$. Extraction of the $[Si_3O_9]^{6-}$ ring

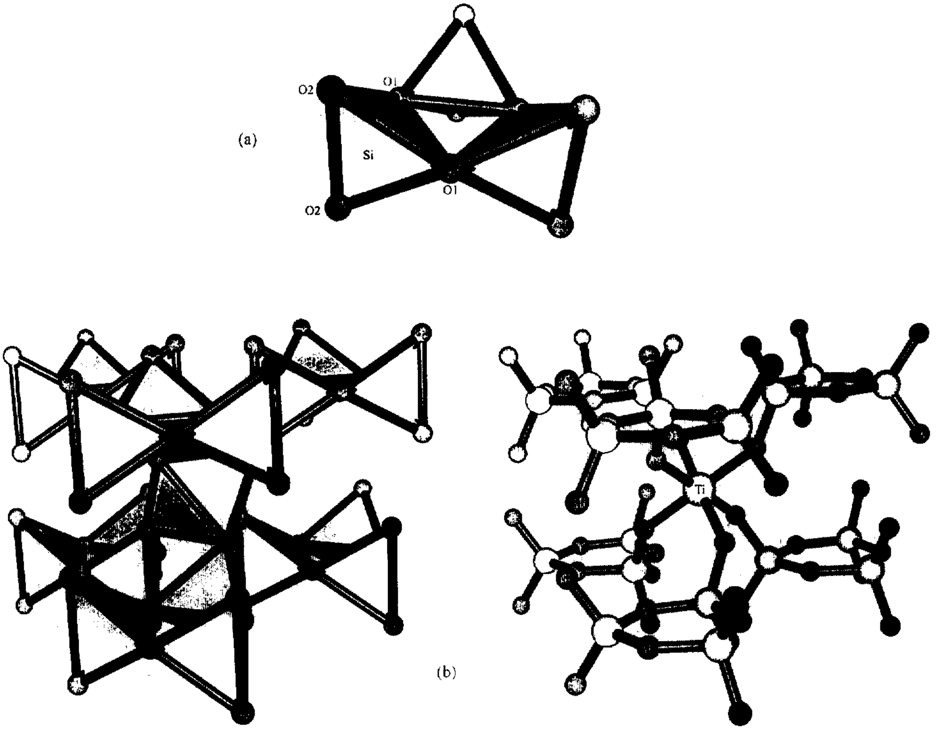

Fig. 11. Retrosynthesis of the crystal structure of benitoite $BaTiSi_3O_9$. (a) The trimeric Si_3O_9 ring of corner-sharing SiO_4 tetrahedra. (b) Model $[Ti(Si_3O_9)_6]^{32-}$ cluster extracted from the network with monodentate coordination mode for the Si_3O_9 rings.

from the network (PEB = +34 eV) leads to $\Delta q/q = 15\%$ on O1 and $\Delta q/q = 36\%$ on O2. These values mean that here it is not possible to decorrelate the trimeric ring from the titanium atoms. Let us investigate the following retrosynthetic sequence:
(1) generation of a TiO_6 octahedron;
(2) addition of silicon atoms directly bonded to oxygen atoms;
(3) addition of oxygen atoms directly bonded to silicon atoms;
(4) addition of silicon atoms directly bonded to oxygen atoms; and
(5) addition of oxygen atoms directly bonded to silicon atoms.
The cluster obtained in this way is displayed in Fig. 11(b) and has $[Ti(Si_3O_9)_6]^{32-}$ stoichiometry. Fig. 11(b) shows that each oxygen atom of the TiO_6 octahedron comes from an unshared corner of a trimeric $[Si_3O_9]^{6-}$ ring. For the core oxygen atoms of this cluster, we find $\Delta q/q(O1) = 8\%$ and $\Delta q/q(O2) = 3\%$. However, if we limit the retrosynthetic sequence to the first three steps, we obtain a $[Ti(SiO_4)_6]^{20-}$ cluster, and now $\Delta q/q(O1) = 87\%$ against $\Delta q/q(O2) = 1\%$. This clearly shows that the $[Si_3O_9]^{6-}$ ring found in benitoite cannot be considered as a tecton. It is rather formed as a consequence of the hexagonal stacking of monodentate silicated titanium

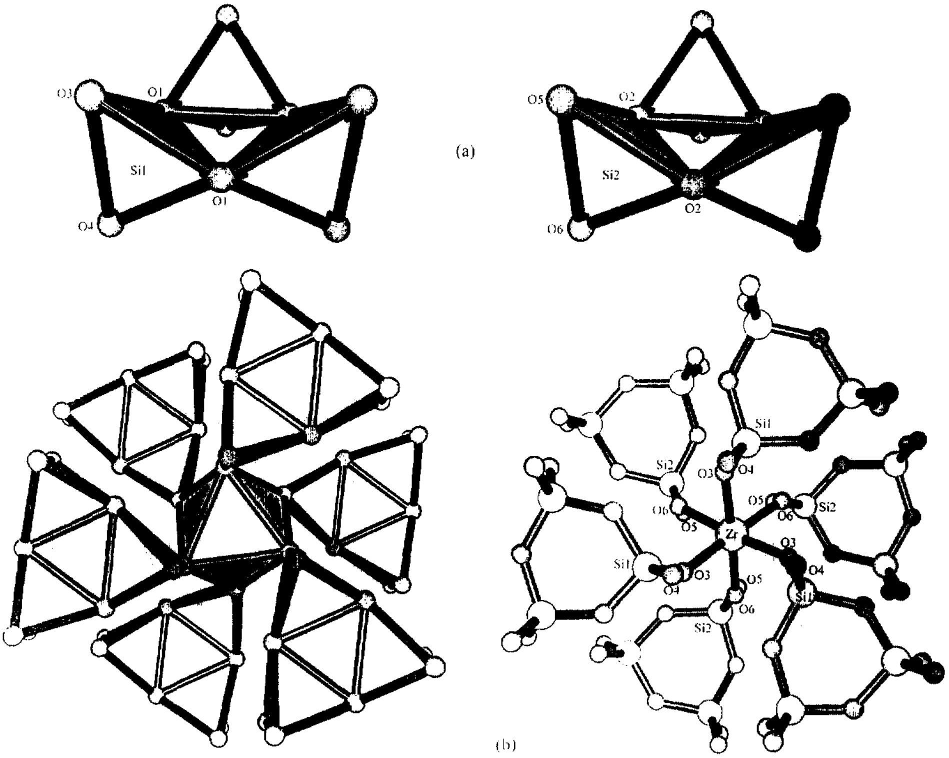

Fig. 12. Retrosynthesis of the crystal structure of wadeite $K_2ZrSi_3O_9$. (a) The two trimeric Si_3O_9 ring of corner-sharing SiO_4 tetrahedra. (b) Model $[Zr(Si_3O_9)_6]^{32-}$ cluster extracted from the network with monodentate coordination mode for the Si_3O_9 rings [cf. Fig. 11(b) for the change in conformation].

complexes, with the barium atoms filling the gaps and providing the necessary reticular energy for crystallization.

If we replace the barium atom in benitoite by two potassium atoms we obtain the wadeite stoichiometry $K_2ZrSi_3O_9$ (space-group P3, $Z=2$, PEB $= -58$ eV, $I=30.3\%$) [60]. This reduction in symmetry leads to the occurrence of two kinds of $[Si_3O_9]^{6-}$ ring [Fig. 12(a)] which cannot be differentiated from the crystalline partial charge distribution: $q(\mathrm{Zr})=1.725\pm0.005$, $q(\mathrm{K})=0.97\pm0.04$, $q(\mathrm{Si1})=q(\mathrm{Si2})=+0.75$, $q[\mu_2\text{-O1}(\mathrm{Si}_2)]=q[\mu_2\text{-O2}(\mathrm{Si}_2)]=-0.59$, $q[\mu_2\text{-O4}(\mathrm{SiZr})]=q[\mu_2\text{-O6}(\mathrm{SiZr})]=-0.68$ and $q[\mu_2\text{-O3}(\mathrm{SiZr})]=q[\mu_2\text{-O5}(\mathrm{SiZr})]=-0.68$. Here also, extracting these two trimeric $[Si_3O_9]^{6-}$ rings from the network (PEB $= +35$ eV) drastically changes the charge distribution: $\Delta q/q(\mathrm{O3,O5})=40\%$, $\Delta q/q(\mathrm{O4,O6})=35\%$ and $\Delta q/q(\mathrm{O1,O2})=17\%$. Applying the same retrosynthetic sequence as in benitoite also leads to a $[Zr(Si_3O_9)_6]^{32-}$ cluster, but with a completely different conformation. In benitoite each $[Si_3O_9]^{6-}$ ring can be eclipsed by another equivalent ring, whereas in wadeite all rings are decaled [Fig. 12(b)]. This difference in conformation is well evidenced by the charge differentials values $\Delta q/q$ which are here found to be less than 4% for all oxygen atoms (O1–O6). If we stop the generation process at the $[Zr(SiO_4)_6]^{20-}$ stage, we find $\Delta q/q$(O1,O2)=93%, $\Delta q/q$(O3,O5)=11% and $\Delta q/q$(O4,O6)=7%. Consequently, it seems that in contrast with the benitoite case, a better charge invariance is obtained by selecting the $[Zr(Si_3O_9)_6]^{32-}$ cluster rather than the smaller $[Zr(SiO_4)_6]^{20-}$ cluster. This could mean that the active tectons of wadeite are zirconium atoms complexed by monodentate trimeric $[Si_3O_9]^{6-}$ rings, whereas those of benitoite should rather be titanium atoms complexed with monodentate $[SiO_4]^{4-}$ monomers. If this interpretation is true, this means that changing the counter-cation may have a deep influence on the crystal growth mechanism, even if the structural influence of the counter-cation seems to be quite negligible.

5.2. *Silicate structures containing the $[Si_4O_{12}]^{8-}$ ring*

We now turn to some tetrameric rings. Such a fully planar ring is found in the crystal structure of synthetic barium copper silicate $BaCuSi_2O_6$ (space group I4/mmm, $Z=4$, PEB= −68 eV, I=41%) [61]. The crystalline charge distribution is found to be q(Ba)= +1.98, q(Cu)= +1.58, q(Si)= +0.87, $q[\mu_2\text{-O2}(Si_2)]=-0.72$ and $q[\mu_2\text{-O1}(SiCu)]=-0.97$. After extraction of the $[Si_4O_{12}]^{8-}$ tetramic ring from the network (Fig. 13), we find $\Delta q/q$(O2)=0% and $\Delta q/q$(O1)=5% with PEB= +50 eV, meaning that such a ring is beyond any doubt a perfect tecton for this phase.

The $[Si_4O_{12}]^{8-}$ tetramic ring found is tugtupite $Na_4AlBeSi_4O_{12}Cl$ (space group $I\bar{4}$, $Z=2$, PEB= −151 eV, I=42.4%) is not planar [Fig. 14(a)], displaying a boat-shaped conformation [62]. The crystalline charge distribution is found to be q(Be)= +1.96, q(Al)= +1.70, q(Na)= +1.00, q(Si)= +0.94, $q(\mu_4\text{-ClNa}_4)=-0.93$, $q[\mu_3\text{-O1}(Si_2Na)]=-0.69$, $q[\mu_3\text{-O3}(SiAlNa)]=-0.89$ and $q[\mu_4\text{-O2}(SiBeNa_2)]=-1.04$. Extraction of the $[Si_4O_{12}]^{8-}$ tetramic ring (PEB= +64 eV) from the network leads to $\Delta q/q$(O1)=4%, $\Delta q/q$(O2)=6% and $\Delta q/q$(O3)=10%, showing that shared corners are not greatly affected by the removal of the network. However, a better charge invariance is found by considering a $[SiAlBeO_9]_4^{36-}$ cluster including all four-fold coordinated atoms which can be generated using the following retrosynthetic sequence:

(1) generation of a $[Si_4O_{12}]^{8-}$ tetramic ring by masking Na, Al, Be and Cl atoms;
(2) addition of Al and Be atoms directly bonded to the ring; and
(3) addition of oxygen atoms directly bonded to atoms Al and Be.

The resulting cluster is displayed in Fig. 14(b), leading to $\Delta q/q$(O1)=6%, $\Delta q/q$(O2)=4% and $\Delta q/q$(O3)=1%. The tecton which emerges from this analysis is a linear trimer $[O_3AlOSiO_3BeO_3]^{11-}$ [Fig. 14(d)] acting as a bidentate ligand towards a NaCl ion-pair on the beryllium side and as a monodentate ligand towards another NaCl ion-pair on the aluminum side. With such a mechanism, the formation of the $[Si_4O_{12}]^{8-}$ ring should be the consequence of tetrahedral stacking around chlorine atoms of such trimeric tectons.

The chair-shaped $[Si_4O_{12}]^{8-}$ ring conformer is found in the crystal structure of papagoite $CaCuAlSi_2O_6(OH)_3$ [Fig. 15(a)] [63]. However, as hydrogen atoms have not been located in the refinement, we were not able to perform the retrosynthesis of this crystal structure. The only thing we can say is that this chair-shaped conformer

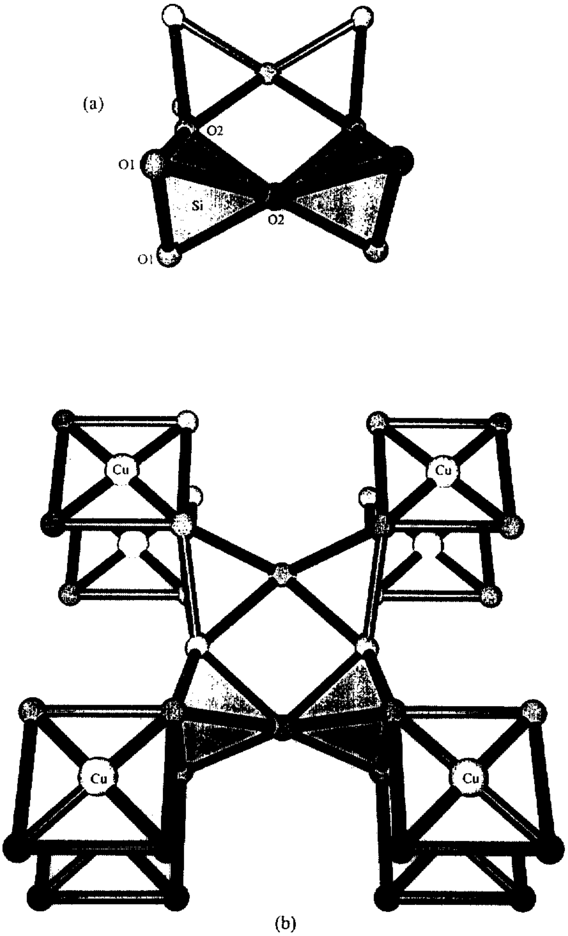

Fig. 13. Retrosynthesis of the crystal structure of synthetic $BaCuSi_2O_6$. (a) The tetrameric Si_4O_{12} ring of corner-sharing SiO_4 tetrahedra. (b) Stacking of square-planar CuO_4 groups with a tetrameric Si_4O_{12} ring.

appears to be 1 eV more stable (PEB = +63 eV) that the boat-shaped conformer found in tugtupite. The same problem of the localization of hydrogen atoms arises with the crystal structure of the synthetic phase $K_4(HSiO_3)_4$, which contains the double chair-shaped $[Si_4O_{12}]^{8-}$ ring conformer [Fig. 15(b)] [64]. The rather low PEB value found for the extracted ring (+55 eV) should be taken with caution owing to the occurrence of unusually short Si–O bonds (156 ± 2 pm) in this unrefined crystal structure. Finally, a perfectly planar $[Si_4O_{12}]^{8-}$ ring has been observed in the crystal structure of $CsSbO_2SiO_3$ with PEB = +62 eV [65]. Here also it was not possible to perform retrosynthesis of this structure owing to some disorder among the caesium and oxygen positions.

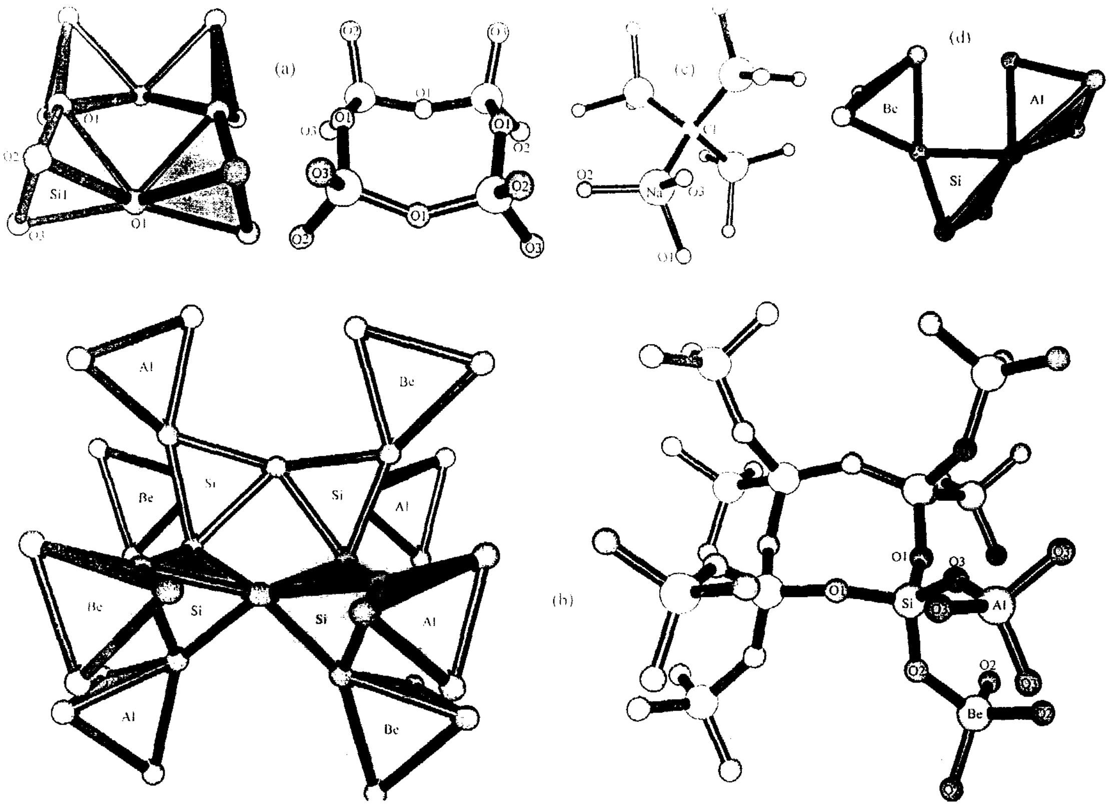

Fig. 14. Retrosynthesis of the crystal structure of tugtupite $Na_4AlBeSi_4O_{12}Cl$. (a) The tetrameric Si_4O_{12} ring of corner-sharing SiO_4 tetrahedra. (b) Model cluster $[SiAlBeO_9]_4^{36-}$ extracted from the network. (c) Tetrahedral coordination of sodium and chlorine atoms in tugtupite. (d) The trimeric linear $AlBeSiO_{10}$ tecton.

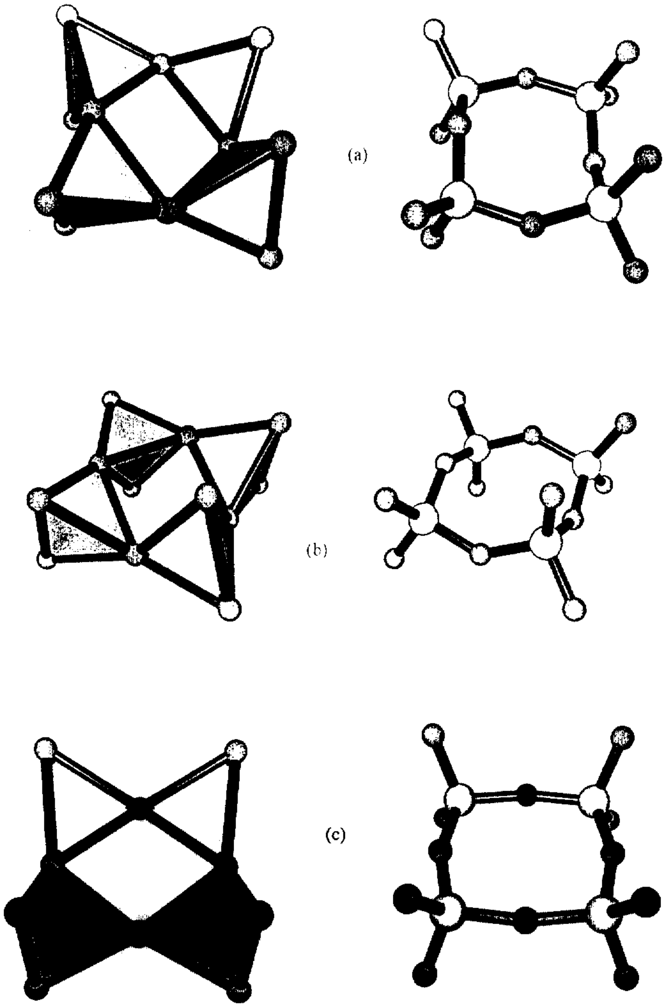

Fig. 15. Silicate structures containing insular Si_4O_{12} rings of corner-sharing tetrahedra for which we were unable to perform retrosynthesis owing to missing hydrogen atom coordinates and/or cationic disorder. (a) Tetrameric ring in papagoite $CaCuAlSi_2O_6$. (b) Tetrameric ring in synthetic $K_4(HSiO_4)_4$. (c) Tetrameric ring in $CsSbO_2SiO_3$.

5.3. Silicate structures containing the $[Si_6O_{18}]^{12-}$ ring

To the best of our knowledge, there are no examples of crystal structures containing an $[Si_5O_{15}]^{10-}$ ring. This confirms the instability of a linear chain-like $[Si_5O_{16}]^{12-}$ species whose cyclization would lead to such a pentameric ring. However, hexameric $[Si_6O_{18}]^{12-}$ rings have been observed in the crystal structure of numerous precious minerals, raising the question of the mechanism of the formation of such rings. The most symmetrical and planar hexameric ring is found in the crystal structure of beryl $Al_2Be_3(SiO_3)_6$ (space group P6/mcc, $Z=2$, PEB $= -303$ eV, $I=48\%$) [66]. The crystalline charge distribution is $q(\mathrm{Be})=+1.99$, $q(\mathrm{Al})=+1.97$, $q(\mathrm{Si})=+1.24$, $q[\mu_2\text{-O1}(\mathrm{Si_2})]=-0.69$ and $q[\mu_3\text{-O2}(\mathrm{SiBeAl})]=-1.10$. Surprisingly enough, extraction of the hexameric $[Si_6O_{18}]^{12-}$ ring (PEB $= +134$ eV) does not lead to huge charge variations: $\Delta q/q(\mathrm{O1})=6\%$ and $\Delta q/q(\mathrm{O2})=8\%$ [Fig. 16(a)]. Association of 12 BeO_4 tetrahedra to this ring is of no help, as this leads to a $[Be_2SiO_9]_6^{60-}$ cluster with $\Delta q/q(\mathrm{O1})=11\%$ and $\Delta q/q(\mathrm{O2})=16\%$. Association of 12 AlO_6 octahedra to the ring is more favorable as it leads to a $[Al_2SiO_{13}]_6^{96-}$ cluster, where $\Delta q/q$ (O2) $=8\%$ but $\Delta q/q(\mathrm{O1})=13\%$. Finally, association of 12 BeO_4 tetrahedra and 12 AlO_6 octahedra leading to a $[Be_2Al_2SiO_{13}]_6^{72-}$ cluster gives the best charge invariance with $\Delta q/q(\mathrm{O1})=4\%$ and $\Delta q/q(\mathrm{O2})=7\%$. The most invariant oxygen atom is then found to be O1, which is common to two SiO_4 tetrahedra within the hexameric ring. As the simultaneous association of BeO_4 tetrahedra and AlO_6 octahedra leads to a better charge invariance, and as the formation of a

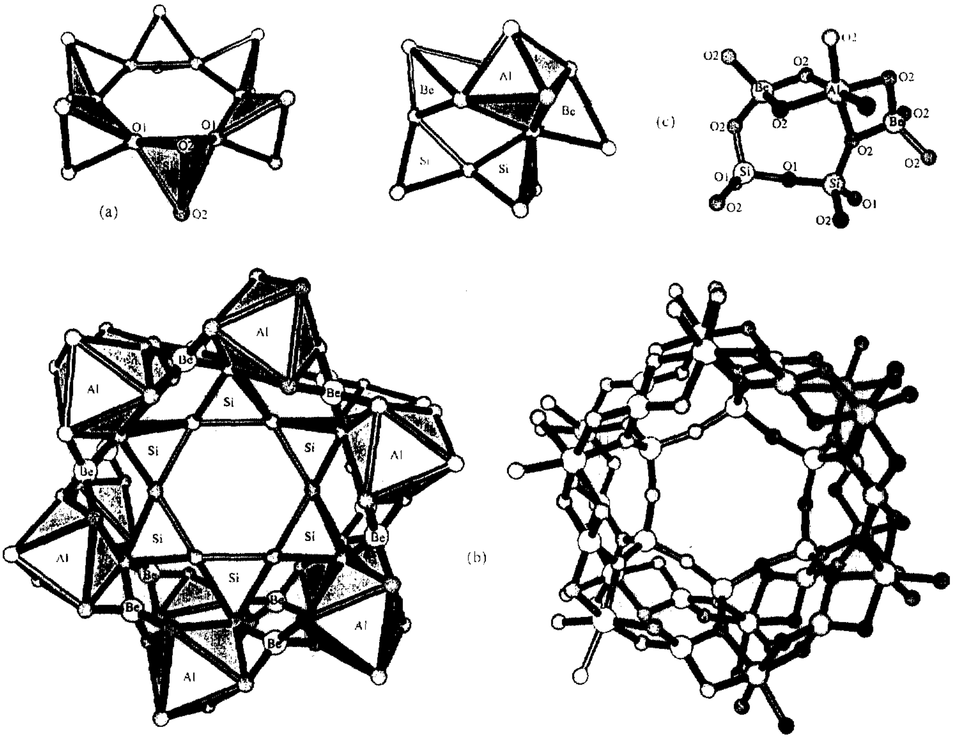

Fig. 16. Retrosynthesis of the crystal structure of beryl $Al_2Be_3(SiO_3)_6$. (a) The hexameric Si_6O_{18} ring of corner sharing SiO_4 tetrahedra. (b) Model cluster $[Be_2Al_2SiO_{13}]_6^{72-}$ extracted from the network. (c) The tetrameric linear $Be_2Si_2O_{13}$ tecton acting as a double bidentate ligand towards aluminum atoms.

hexameric $[Si_6O_{18}]^{12-}$ ring from the cyclization of a linear $[Si_6O_{19}]^{14-}$ oligomer is very unlikely, the most plausible retrosynthetic pathway should be the hexagonal packing of monomeric aluminum atoms complexed by tetrameric species $[O_3BeOSiO_3SiO_3BeO_3]^{14-}$ acting as double bidentate ligands through the beryllium ends [Fig. 16(c)].

A ditrigonal distortion of the hexameric ring [Fig. 17(a)] is found in the crystal structure of tourmaline $NaMg_3B_3Al_6Si_6O_{30}(OH)$ [67] and buergerite $NaFe_3B_3Al_6Si_6O_{30}F$ (space group R3m, $Z=3$, PEB $= -352$ eV, $I=40.7\%$) [68]. Table 10 gives the whole crystalline charge distribution for this very beautiful crystal structure. Obviously, the hexameric $[Si_6O_{18}]^{12-}$ ring (PEB $= +144$ eV) cannot be considered as a tecton for this structure in view of the large $\Delta q/q$ ratios. Some counter-cations should then be associated with the hexameric ring, and the following retrosynthetic sequence was applied:

(1) generation of a $[Si_6O_{18}]^{12-}$ ring by considering only silicon or oxygen atoms;
(2) addition of Al and Fe atoms directly bonded to oxygen atoms; and
(3) addition of oxygen and fluorine atoms directly bonded to Fe and Al atoms.

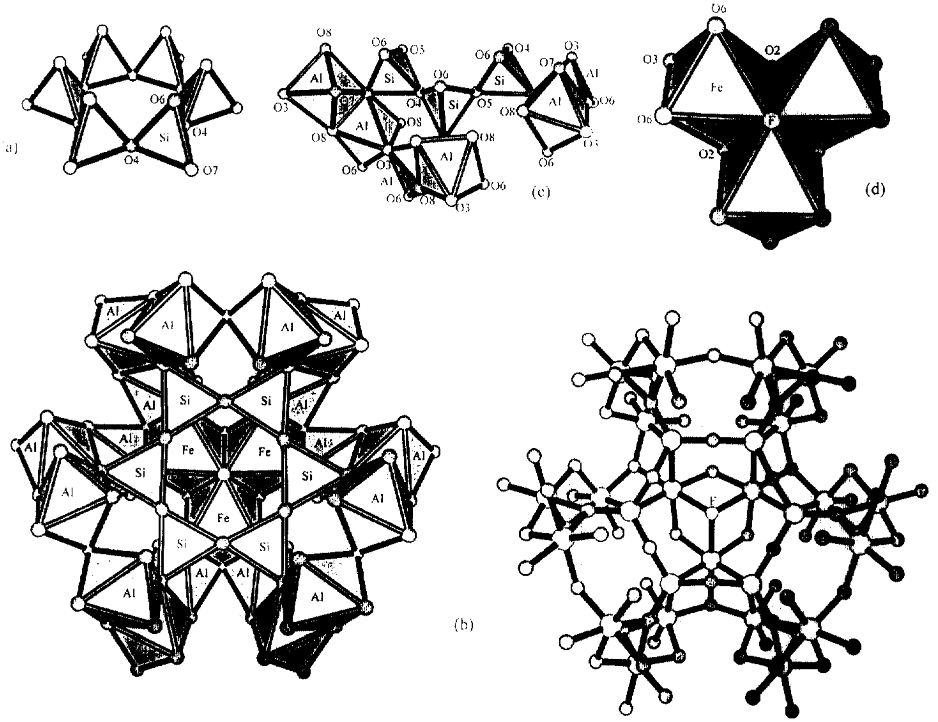

Fig. 17. Retrosynthesis of the crystal structure of buergerite $NaFe_3B_3Al_6Si_6O_{30}F$. (a) The hexameric Si_6O_{18} ring of corner sharing SiO_4 tetrahedra. (b) Model $[FC_3Al_{18}Si_6O_{87}F]^{88-}$ cluster extracted from the network. (c) The octahedral edge-sharing Al_2O_{10} dimers complexed by a linear Si_3O_{10} trimer. (d) The octahedral corner-sharing Fe_3FO_{12} trimer which can be associated to boron atoms and aluminosilicate tectons of (c) to form the buergerite framework.

Table 10

Crystalline partial charges distribution in buergerite $NaFe_3B_3Al_6Si_6O_{30}F$ and $\Delta q/q$ ratios (%) after extraction of the hexameric $[Si_6O_{18}]^{12-}$ non-planar ring (middle column) or of a $[Fe_3Al_{18}Si_6O_{87}F]^{88-}$ cluster (last column)

Crystalline site	Atomic partial charge q	$\Delta q/q$ in $[Fe_3Al_{18}gSi_6O_{87}F]^{88-}$ (%)
μ_3-O(BAl_2)	O8 = −1.06	1
μ_3-O($SiAl_2$)	O7 = −0.86 (32%)	5
μ_3-O($FeAl_2$)	O3 = −0.79	41
μ_3-O(SiAlFe)	O6 = −0.70 (17%)	14
μ_4-O($NaBFe_2$)	O2 = −0.70	1
μ_3-O($NaSi_2$)	O4 = −0.62 (13%)	5
μ_3-O($NaSi_2$)	O5 = −0.59 (17%)	5
μ_3-F(Fe_3)	F = −0.52	15
FeO_5F	Fe = +0.71	–
NaO_6	Na = +0.99	–
SiO_4	Si = +1.00	–
BO_3	B = +1.25	–
AlO_6	Al = +1.92	–

The resulting cluster has $[Fe_3Al_{18}Si_6O_{87}F]^{88-}$ stoichiometry [Fig. 17(b)] with the associated $\Delta q/q$ ratios given in Table 10. Obvious corner stones are found to be oxygen atoms O2 and O8, which both belong to the coordination sphere of trigonal BO_3 groups. Starting from atom O2 we can reach a boron atom, two iron atoms or a sodium atom. As boron and sodium atoms have not been included in the generation sequence, this means that the tecton should involve the two remaining iron atoms which are bonded to atoms O3 (194 pm), O6 (two at 199 pm) and F (211 pm). As can be seen from Table 10, these three atoms have $\Delta q/q$ ratios of higher than 10%. Consequently, by limiting our investigations to atom O2, a cyclic trimer $[(O_3Fe)_3FO_3]$ of three corner-sharing FeO_5F octahedra having the fluorine atom in common emerges from the structure. It is rather pleasant to find that such a topological arrangment of three octahedra is a basic feature of many iron-based polyanions [69]. Having identified a first tecton, let us now have a look at the second invariant oxygen atom, i.e. O8. From here we can again reach a boron atom or two aluminum atoms. As before, we may ignore this boron atom and look at the coordination sphere of AlO_6 octahedra. Here we find two O7 atoms (189 and 198 pm), two O8 atoms (189 and 193 pm), one O3 atom (190 pm) and one O6 atom (192 pm). As before, discarding these last two atoms, an edge-sharing octahedral $[(O_4Al)_2O_2]$ dimer emerges as atoms O7 display rather low $\Delta q/q$ ratios. Again, it is satisfactory to find that this structural unit may be found in many oxide-based aluminum compounds. From Table 10, only atoms O4 and O5 remain which have $\Delta q/q$ lower than 10%. Starting from these two atoms, a linear $[Si_3O_{10}]$ tecton emerges which is linked to the $[(O_4Al)_2O_2]$ tecton through atom O7 and to the $[(O_3Fe)_3FO_3]$ tecton through atom O6. The planar trigonal coordination sphere of the remaining boron atom atom then appears to involve two edge-sharing octahedral $[(O_4Al)_2O_2]$ tectons and one corner-sharing octahedral $[(O_3Fe)_3FO_3]$ tecton. In

Table 11
Distribution of crystalline partial charges in dioptase $CuSiO_3.H_2O$ or $CuSiO_3$ and $\Delta q/q$ ratios (%) after extraction of hexameric $[Si_6O_{18}]^{12-}$ non-planar rings

Crystalline site	Partial charge in $CuSiO_3.H_2O$	Partial charge in $CuSiO_3$
μ_3-O($SiCu_2$)	O2 = −1.03 (0%)	O3 = −1.09 (12%)
μ_3-O($SiCu_2$)	O3 = −1.01 (5%)	O2 = −1.07 (5%)
μ_2-O(H_2)	O4 = −0.57	–
μ_2-O(Si_2)	O1 = −0.54 (17%)	O1 = −0.61 (7%)
H	H1 = H2 = +0.10	–
SiO_4	Si = +0.97	Si = +0.94
CuO_4	Cu = +1.98	Cu = +1.83

tourmaline, iron and fluorine atoms are replaced by magnesium atoms and a hydroxyl group, forming a $[(O_3Mg)_3(OH)O_3]$ tecton. As hydrogen atoms have not yet been localized in this structure, it is not possible to check this point further.

Another kind of hexameric $[Si_6O_{18}]^{12-}$ ring is found in the crystal structures of dioptase minerals $CuSiO_3.H_2O$ (blue hydrated form) [70] and $CuSiO_3$ (black anhydrous form) [71]. Table 11 compares the distribution of crystalline partial charges in the hydrated form (space group $R\bar{3}$, $Z = 18$, PEB = −44 eV, $I = 41.2\%$) and in the anhydrous form (space group $R\bar{3}$, $Z = 18$, PEB = −41 eV, $I = 44.6\%$). In both phases, the lowest $\Delta q/q$ ratios are found for just one of the two unshared oxygen atoms (O2) of the hexameric $[Si_6O_{18}]^{12-}$ rings (PEB = +151 eV) [Fig. 18(a) and (b)]. In the hydrated form, it is the second unshared oxygen atom (O3) which has the lowest $\Delta q/q$ ratio, whereas in the anhydrous form it is the corner-sharing oxygen atom (O1). This sensitivity of shared oxygen atoms to water removal in the hydrated phase may be attributed to a very particular hydrogen bond pattern. Fig. 18(c) shows the result of perfoming an iterative search at 2.0 Å involving only atoms O1, O4, H1 and H2, which leads to a finite cluster having the stoichiometry $[O_6(H_2O)_6]$ with $d(O4–O4) = 269$ pm, $d(O1–O4) = 283$ pm, $\theta(O4–H1–O4) = 154°$ and $\theta(O1–H2–O4) = 172°$. In the anhydrous phase, this hydrogen bond pattern does not exist, and accordingly the $\Delta q/q$ ratio of oxygen atom O1 becomes of the same order of magnitude as that of atom O2. Another interesting fact is that association of square-planar CuO_4 polyhedra to the hexameric rings of either hydrated or anhydrous phases leading to $[Cu_3SiO_9]_6^{48-}$ clusters [Fig. 18(d)] does not lead to a better charge invariance. This means that hexameric $[Si_6O_{18}]^{12-}$ rings should be considered as valuable tectons for the dioptase phases. Consequently, they should have been formed prior to crystal growth through condensation of three $[Si_2O_7]$ dimers or of two $[Si_3O_{10}]$ linear trimers. Owing to the occurrence of just one kind of corner-sharing oxygen atom in the resulting hexameric ring, it is not possible to decide which pathway is most likely to occur from the crystal structure. However, for obvious statistical reasons, i.e. the meeting of two trimers having a much higher probability than the simultaneous meeting of three dimers, we prefer to explain the formation of a $[Si_6O_{18}]^{12-}$ ring through the dimerization of linear $[Si_3O_{10}]$ trimers.

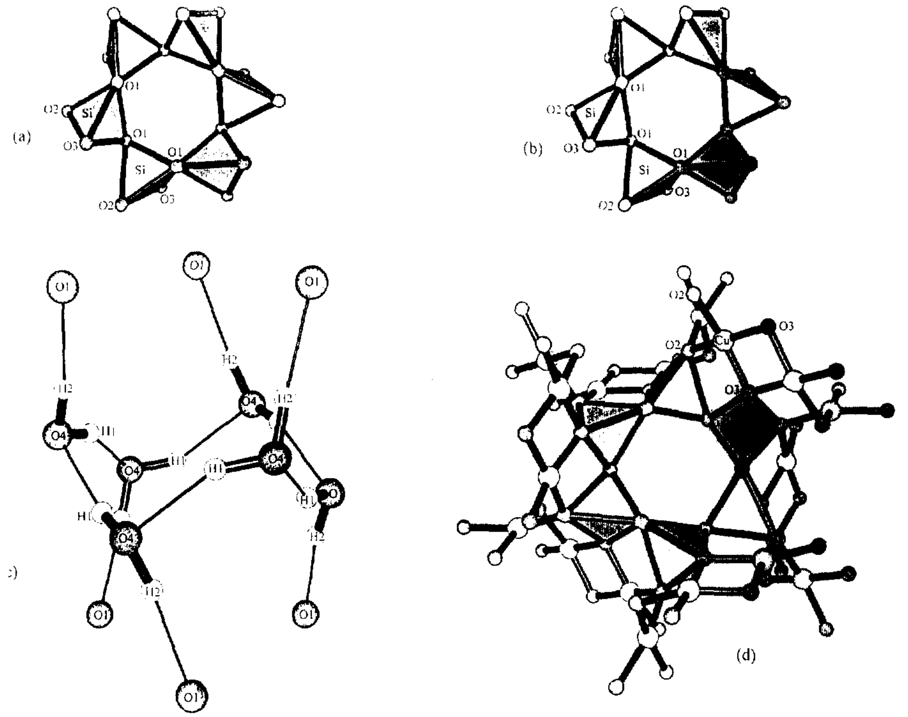

Fig. 18. Retrosynthesis of the crystal structures of blue $CuSiO_3.H_2O$ and black $CuSiO_3$ dioptase. (a) The tetrameric Si_6O_{18} ring of corner-sharing SiO_4 tetrahedra in blue dioptase. (b) The tetrameric Si_6O_{18} ring of corner-sharing SiO_4 tetrahedra in black dioptase. (c) The hydrogen bond pattern found in blue dioptase. (d) A $[Cu_3SiO_9]_6^{48-}$ cluster extracted from the network showing the stacking of quasi square-planar CuO_4 groups with a tetrameric Si_6O_{18} ring.

Hexameric $[Si_6O_{18}]^{12-}$ rings are also found in the crystal structures of lovozerite $Na_4Zr_2Si_{12}O_{30}.6H_2O.NaOH$ [Fig. 19(a)] [72] and imandrite $Na_{12}Ca_3Fe_2(Si_6O_{18})_2$ [Fig. 19(b)] [73]. The non-localization of the hydrogen atoms in lovozerite and the disordering of calcium atoms in imandrite prevents us from performing the retrosyntheses of these two rings, which seem ad oculos to be formed from the condensation of two linear $[Si_3O_{10}]$ trimers. The hexameric ring in the imandrite structure has a PEB value of +146 eV, which is very similar to the value found in buergerite. Still larger silicate rings have been characterized in the solid state. The minerals of the muirite family $Ba_{10}(Ca,Mn,Ti)_4Si_8O_{24}(Cl,OH,O)_{12}.4H_2O$ contain an octameric $[Si_8O_{24}]^{16-}$ ring with PEB = +256 eV [Fig. 19(c)] [74]. Those of the eudialyte family $Na_{12}Ca_6Fe_3Zr_3Si_{24}O_{66}(Cl,OH)_8$ are characterized by the occurrence within the same crystal structure of both nonameric $[Si_9O_{27}]^{18-}$ (PEB = +302 eV) and trimeric $[Si_3O_9]^{6-}$ rings (PEB = +33 eV) [Fig. 19(d)] [75]. Here the non-localization of hydrogen atoms and cationic disorder prevents us from checking whether the octameric ring of muirite is built from the condensation of four $[Si_2O_7]$ dimers or two $[Si_4O_{13}]$ linear tetramers, or whether the nonameric ring of eudialyte comes

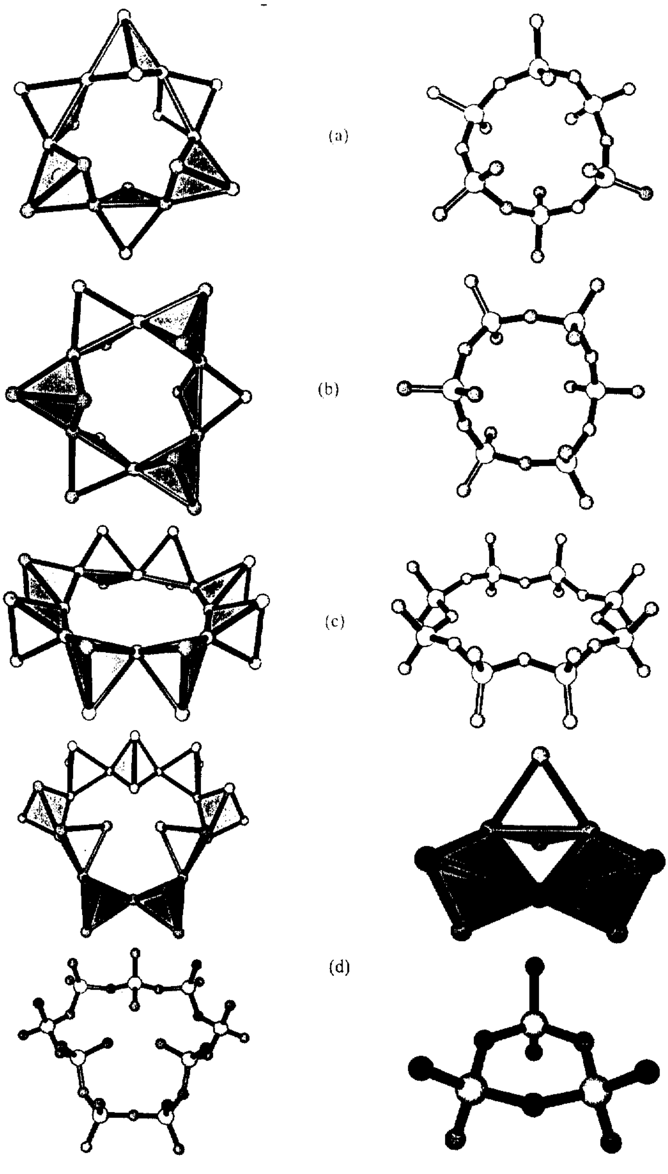

Fig. 19. Silicate structures containing insular Si_nO_{3n} rings of corner-sharing tetrahedra for which we were unable to perform retrosynthesis owing to missing hydrogen atom coordinates and/or cationic disorder. (a) Hexameric ring in lovozedte $Na_4Zr_2Si_{12}O_{30}.6H_2O.NaOH$. (b) Hexameric ring in imandrite $Na_{12}Ca_3Fe_2(SiO_{18})_2$ (c) Octameric ring in muirite $Ba_{10}(Ca,Mn,Ti)_4Si_8O_{24}(Cl,OH,O)_{12}.4H_2O$. (d) Trimeric and nonameric rings in eudialyte $Na_{12}Ca_6Fe_3Zr_3Si_{24}O_{66}(Cl,OH)_8$.

from the condensation of three linear $[Si_3O_{10}]$ trimers. The answer to these fascinating questions will have to wait for better crystal structure refinements and the localization of all atoms. However, Fig. 20 shows that as for linear oligomers, there should also

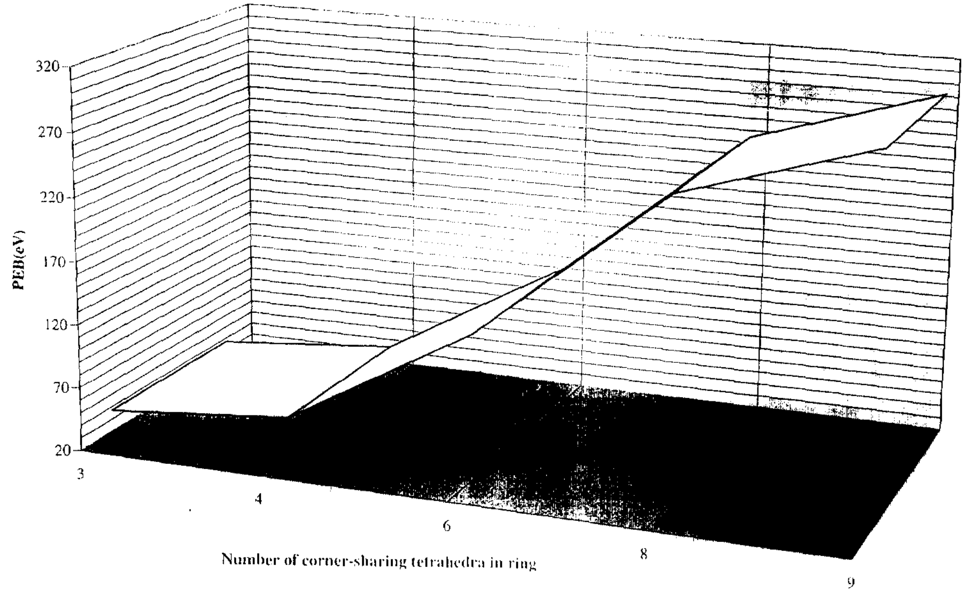

Fig. 20. Variation of the PEB of a growing naked silicate ring $[Si_nO_{3n}]^{2n-}$ as a function of the number of corner-sharing tetrahedron within the ring.

be a limit to the formation of larger and larger $[Si_nO_{3n}]^{2n-}$ rings owing to the huge increase in PEB values when going from $n=3$ to $n=9$.

5.4. Silicate structures containing silicate cages

Condensation of two rings to form a polysilicate cage appears to be a very efficient way of removing electrostatic pressure. The formation of a hexameric $[Si_6O_{15}]^{6-}$ cage has been observed in the crystal structure of $[Ni(en)_3]Si_2O_5.8.7H_2O$ [Fig. 21(a)] [76]. The PEB value of this cage is found to be +4 eV, in contrast to that of two isolated trimeric $[Si_3O_9]^{6-}$ rings, which is about +60 eV. Much more interesting is the negative PEB value of −2 eV found for an octameric $[Si_8O_{20}]^{8-}$ cage extracted from the crystal structure of $[N(CH_3)_4]_8Si_8O_{20}.64.8H_2O$ [Fig. 21(b)] [77]. This good electrostatic stability of double four-membered rings relative to other polysilicates could help to explain the experimental evidence that the frameworks of the lowest density (zeolite-type tetrahedral nets) are those with a maximum number of four-membered rings [78]. Finally, the presence of dodecameric $[Si_{12}O_{30}]^{12-}$ cages with PEB = +58 eV has been evidenced in the crystal structures of milarite $KCa_2(AlBe_2)Si_{12}O_{30}.H_2O$ and osumilite $(K,Na,Ca)(Mg,Fe)_2(Al,Fe)_3Si_{12}O_{30}.H_2O$ [Fig. 21(c)] [79]. It is highly probable that a much lower PEB value would have been obtained for these huge cages if the water molecule trapped inside the cages had been included. Consequently cage compounds, in contrast to chain-like or ring oligomers, do not have to be heavily solvated to exist as rather stable chemical species. However, the retrosynthesis of all these structures is not yet possible owing

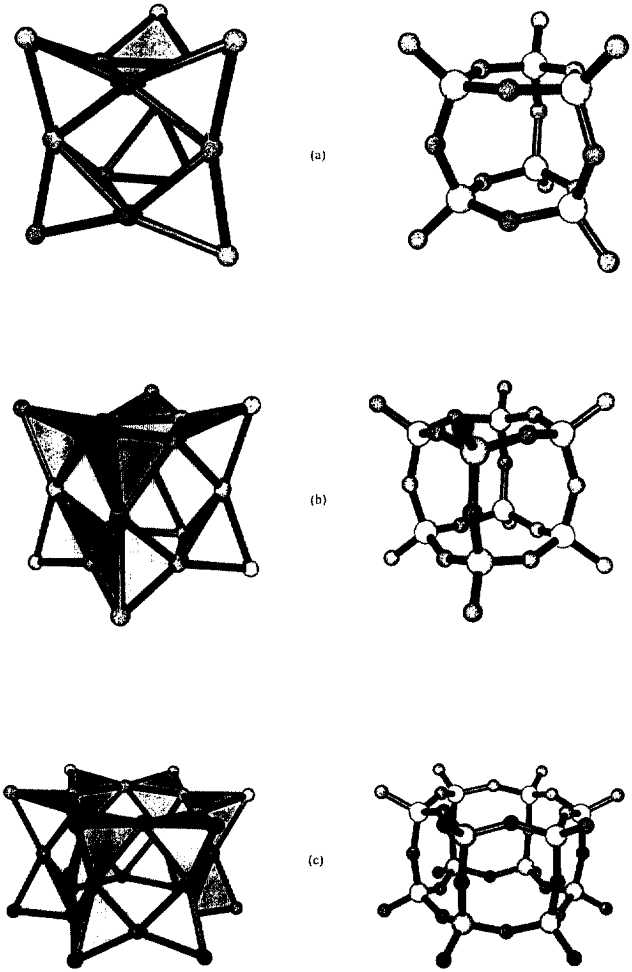

Fig. 21. Silicate structures containing insular silicated cages of corner-sharing tetrahedra for which we were unable to perform retrosynthesis owing to missing hydrogen atom coordinates and/or cationic disorder. (a) Double three-membered ring in synthetic $[Ni(en)_3]Si_2O_5.8.7H_2O$. (b) Double four-membered ring in synthetic $[N(CH_3)_4]8Si_8O_{20}.64.8H_2O$. (c) Double six-membered ring in milarite $KCa_2(AlBe_2)Si_{12}O_{30}.H_2O$ and osumilite $(K,Na,Ca)(Mg,Fe)_2(Al,Fe)_3Si_{12}O_{30}.H_2O$.

to the huge amount of unlocalized molecules or to the presence of disorder in the unit cell.

6. Conclusion

This paper is a first foray into the domain of the retrosynthesis of inorganic crystal structures. The choice of 0D nesosilicate or 1D inosilicate structures containing chains, rings or cages of SiO_4 tetrahedra was made in order to check the validity of the atomic charge invariance upon extraction of a cluster from the crystalline network. The results obtained are quite satisfactory, as in most cases it is possible to identify small groups of atoms (tectons) from which the formation of the whole crystal structure can readily be understood. Uncomplexed SiO_4 monomers seem to be responsible for the crystalline growth of akermanite $Ca_2Si_2O_7$, rankinite $Ca_3Si_2O_7$, barylite $BaBe_2Si_2O_7$, $RE_2Si_2O_7$ (RE = Y, Gd, Sm), kilchoanite $Ca_3Si_2O_7$, diopside $CaMgSi_2O_6$ and fluortremolite $Ca_2Mg_5Si_8O_{22}F$. Uncomplexed Si_2O_7 dimers are involved in the crystal growth of thortveite $Sc_2Si_2O_7$, $RE_2Si_2O_7$ (RE = Er, Yb), enstatite $MgSiO_3$ and for the synthetic phases $Li_6Si_2O_7$, $Ag_6Si_2O_7$ and $BaCu_2Si_2O_7$. Uncomplexed linear $[Si_3O_{10}]$ trimers are found to be tectons for synthetic $Na_2Ca_3Si_3O_{10}$ or for β-wollastonite $CaSiO_3$, but also for synthetic $Ag_{10}Si_4O_{13}$ after association with a SiO_4 monomer. Uncomplexed metasilicate rings emerges also as tectons from α-wollastonite $CaSiO_3$ (Si_3O_9), synthetic $BaCuSi_2O_6$ (Si_4O_{12}) and dioptase $CuSiO_3$ or $CuSiO_3.H_2O$ (Si_6O_{18}). Crystalline growth could also involve silicate chains or rings acting as ligands towards other chemical species. Complexed monomers $TiSiO_4$ or $SbSiO_4$ emerge from the retrosynthesis of benitoite $BaTiSi_3O_9$ or synthetic $CsSbO(SiO_3)_2$. Both complexed dimers $Mn_2Si_2O_7$ and linear trimers $Mn_3Si_3O_{10}$ are responsible for the growth of rhodonite $MnSiO_3$, while the growth of pyroxmangite $MnSiO_3$ involve complexed linear trimers $Mn_3Si_3O_{10}$. Association of boron atoms with octahedral $[Al_2O_{10}]$ dimers complexed by linear $[Si_3O_{10}]$ trimers and octahedral cyclic $[Fe_3FO_{12}]$ trimers leads to the beautiful crystal structure of buergerite $NaFe_3B_3Al_6Si_6O_{30}F$. Substitution of silicon by aluminum or beryllium is possible. Thus, association of NaCl species with $SiBeAlO_{10}$ linear trimers was found in tugtupite $Na_4AlBeSi_4O_{12}Cl$. Beryl $Al_2Be_3(SiO_3)_6$ is instead formed through complexation of aluminum atoms by linear $Si_2Be_2O_{13}$ tetramers. We have not been able to perform retrosynthesis of the following phases: ardennite with linear Si_3O_{10} trimers, papagoite and synthetic $CsSbO_2SiO_3$ with Si_4O_{12} rings, lovozerite and imandrite with Si_6O_{18} rings, muirite with Si_8O_{24} rings, eudialyte with Si_9O_{27} rings, $[Ni(en)_3]Si_2O_5.8.7H_2O$ with Si_6O_{15} cages, $[N(CH_3)_4]_8Si_8O_{20}.64.8H_2O$ with Si_8O_{20} cages, milarite and osumilite with $Si_{12}O_{30}$ cages owing to the non-localization of hydrogen atoms or to the occurence of cationic disorder. However, the failure to detect any linear oligomer $[Si_nO_{3n+1}]^{(2n+2)-}$ with $n>4$ or huge $[Si_nO_{3n}]^{2n-}$ rings ($n>9$) in solution or in the solid state is clearly interpreted as the consequence of very unfavorable electrostatic balances (PEB > +100 eV) for these species. In all cases, the number of non-oxygen atoms in the supposed tectons was found to be less than five, and the topological association of the constituting polyhedra was understandable in terms of the well-known molecular coordination chemistry of the various central atoms. It is a very important result that even very complex crystal structures such as those of rhodonite or buergerite can be readily reduced to the association of very simple tectons obeying the laws of coordination chemistry. Obviously, we do not pretend to have demonstrated the real chemical existence of these tectons or elucidated the detailed molecular mechanisms of crystalline growth, but just to have given some new plausible synthetic paths which remain to be supported by any future experimental work in this field.

Another important point to stress is that all the retrosyntheses described in this paper have been performed on a very modest 66 MHz personal computer. In trivial cases such as $BaCuSi_2O_6$, the whole retrosynthesis took a matter of minutes, whereas for more complex crystal structures (buergerite) it was a matter of a few hours. In all cases, the most time-consuming task was to look in the crystal structure for a good model cluster displaying the highest number of invariant atomic charges, and not the computation of the charge distribution (which was straightforward). This response time of at most a few hours for performing a full crystalline retrosynthesis is obviously very encouraging, and allows still more complex crystal structures to be readily investigated. We have thus started to study by this approach not only the mechanisms of formation of microporous compounds (zeolites, alumino- or gallophosphates), but also try to find a link between the crystallization of huge organic or inorganic supramolecular compounds and the physicochemical conditions imposed on the mother solution. Work is in progress in these directions, but is currently being hampered by the quality of the available structural data. Most of these compounds have very large unit cells containing a huge number of solvent molecules. Consequently, if the topology of the network or of the supramolecular host is well defined, the guest molecules are very often disordered, or worse, have not been localized at all. However, missing or ill-placed hydrogen atoms can be placed individually after a careful examination of the hydrogen bond pattern, while disorder can be removed by applying adequate symmetry masks during the unit-cell generation process. All this preliminary work is currently performed by manual trial and error, which slows down the retrosynthesis of these structures considerably. We are currently modifying our WinPacha GUI interface to handle these cases automatically rather than manually. Interesting preliminary results have already been obtained on zeolite networks and isopolyoxometallates, which will be reported in the near future. Another very promising and exciting development which will considerably speed up the retrosynthesis of these problematic inorganic crystal structures is the determination of crystal structures using experimental X-ray and solid-state NMR data. Having all atoms with integral occupation numbers localized in a correct space group, solid-state chemists could focus on the retrosynthesis of crystal structures alone, without having to spend time on guessing missing atomic coordinates or selecting pertinent symmetry operators.

Appendix

Our theoretical model is based on a functional approach of chemical bonding using atomic charges q and their associated potentials v, which are both first derivatives of the total energy of the system E:

$$q \propto \frac{\partial E}{\partial v} \quad \text{and} \quad v \propto \frac{\partial E}{\partial q}.$$

For a chemical system, $q = Z - N$, where Z is the atomic number and N is the nonintegral number of electrons around the nucleus, while v is a measure of its electronegativity χ. This may be readily understood by looking at a diatomic molecule A–B constrained to have $N=Z_A+Z_B=N_A+N_B$ [80]. For any electron transfer dN from B to A ($dN_A=-dN_B=dN>0$) at the internuclear distance R, the change in the total energy should be:

$$E=f(N_A,N_B,Z_A,Z_B,R)\Rightarrow dE$$
$$=\left[\left(\frac{\partial E}{\partial N_A}\right)_{N_B,R}-\left(\frac{\partial E}{\partial N_B}\right)_{N_A,R}\right]dN+\left(\frac{\partial E}{\partial R}\right)_{N_A,N_B}dR \tag{A.1}$$

For a given distance R ($dR=0$) a spontaneous transfer will occur if $dE<0$ for $dN>0$:

$$\Rightarrow\left(\frac{\partial E}{\partial N_A}\right)_{N_B,R}<\left(\frac{\partial}{\partial N_B}\right)_{N_A,R}\Leftrightarrow\chi_A>\chi_B \quad \text{if } \chi=-\left(\frac{\partial E}{\partial N}\right)=\left(\frac{\partial E}{\partial q}\right)=-\mu_e. \tag{A.2}$$

The last equalities arise from the fact that electronegativity measures the affinity of atoms for electrons [81]. Another consequence of Eq. (A.1) is that if $R=R_e$, the internuclear equilibrium distance, then $dE=dR=0$, i.e. $\chi_A=\chi_B$. This is the electronegativity equalization principle of Sanderson [82], meaning that electronegativity should be considered as the opposite of an electronic chemical potential, i.e. $\mu_e=\partial E/\partial N$ [83]. The relation between this electronic chemical potential and the empirical electronegativity, introduced by Pauling in the 1930s is immediate if we introduce the hardness $\eta=\partial^2E/\partial N^2$ of the system (its softness being $\sigma=1/\eta$):

$$E(N)=E^0(Z)+(N-Z)\left(\frac{\partial E}{\partial N}\right)_{N=Z}$$
$$+\frac{(N-Z)^2}{2!}\left(\frac{\partial^2 E}{\partial N_2}\right)_{N=Z}=E^0(Z)+q\chi^0+\frac{q^2}{2}\eta. \tag{A.3}$$

With χ=-$\partial E/\partial N=\chi^{\circ}+\eta\times q$, and $\chi_A=\chi_B=\langle\chi\rangle$ for a diatomic molecule, we have:

$$\chi_A=\chi_A^0-\eta_A q=\chi_B^0+\eta_B q=\chi_B=\langle\chi\rangle\Leftrightarrow q=\frac{\chi_A^0-\chi_B^0}{\eta_A+\eta_B}, \tag{A.4}$$

i.e. a stabilization energy $\Delta=(E_A-E_A^0)+(E_B-E_B^0)=q(\chi_B^0-\chi_A^{\circ})+q_2(\eta_A+\eta_B)/2$:

$$\Delta=-\frac{(\chi_A^0-\chi_B^0)^2}{\eta_A+\eta_B}+\frac{1}{2}\frac{(\chi_A^0-\chi_B^0)^2}{\eta_A+\eta_B}=-\frac{1}{2}\frac{(\chi_A^0-\chi_B^0)^2}{\eta_A+\eta_B}<0, \tag{A.5}$$

in full agreement with the original Pauling definition [81] if $\eta_A+\eta_B\approx$const. Eq. (A.5) also provides a firm theoretical justification of the empirical HSAB principle (hard and soft acids and bases) introduced empirically by Pearson [84]:

$$\eta_A(\text{soft})+\eta_B(\text{soft})<\eta_A(\text{soft})+\eta_B(\text{hard})\Leftrightarrow\Delta(\text{soft}-\text{soft})<\Delta(\text{hard}-\text{soft}).$$

The other part of the HSAB principle [$\Delta(\text{hard}-\text{hard})<\Delta(\text{hard}-\text{soft})$] comes from the contraction of atomic orbitals in response to an increase in the nuclear effective charge Z^* [85], as with $dZ^*>0$ and $(\partial E/\partial Z^*)<0 \Rightarrow \Delta E=(\partial E/\partial Z_A^*)\,dZ_A^*+(\partial E/\partial Z_B^*)\,dZ_B^*<0$.

The problem of the quantitative evaluation of the hardness parameter may be solved by treating an atom as a sphere with a uniformly distributed electric charge q. If this sphere has a characteristic radius r, then:

$$E(q)=\frac{e^2q^2}{8\pi\epsilon_0 r} \Leftrightarrow \chi=\left(\frac{\partial E}{\partial q}\right)=\frac{e^2q}{4\pi\epsilon_0 r} \quad \text{and} \quad \eta=\left(\frac{\partial^2 E}{\partial q^2}\right)=\frac{e^2}{4\pi\epsilon_0 r}. \tag{A.6}$$

The chemical hardness is then known as soon as the atomic radius has been defined [86].

The link between this functional approach of chemical bonding and the more conventional molecular orbital theory is as follows:

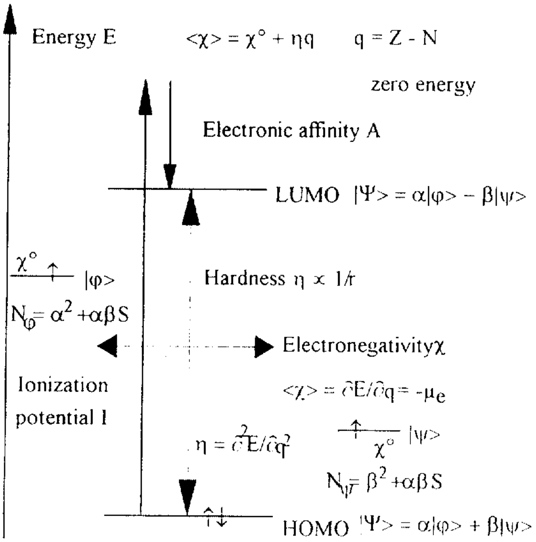

This comes from the Koopman's theorem: $I\approx -E_{\mathrm{HOMO}}$ and $A\approx -E_{\mathrm{LUMO}}$. For a sphere of charge q and characteristic radius r, we have $I=E(q+1)-E(q)$ and $A=E(q)-E(q-1)$:

$$I=\frac{e^2(2q+1)}{8\pi\epsilon_0 r}, \qquad A=\frac{e^2(2q-1)}{8\pi\epsilon_0 r} \Rightarrow \chi=\frac{I+A}{2}, \qquad \eta=I-A$$

in full agreement with the Mulliken definition of orbital electronegativity [87]. Consequently, if electronegativity corresponds to the Fermi level of the electrons in a given chemical system [88,89], its hardness η measures its HOMO–LUMO gap [90].

From a practical point of view, given any system resulting from the association of n atoms with a total electrical charge z, it is possible to write its electronegativity as [91–95]:

$$\chi_i=\langle\chi\rangle=\chi_i^0+\frac{e}{4\pi\epsilon_0 r_i}q_i+\frac{1}{4\pi\epsilon_0}\sum_{j=1}^{n}M_{ij}eq_j \quad \forall i=1,\ldots,n \quad \text{and} \sum_{i=1}^{n}q_i=z, \tag{A.7}$$

where χ_i^0 are the Mulliken electronegativities of the valence orbitals used for chemical bonding [96,97] and r_i is a set of atomic radii modelling the spatial extent of these orbitals. M_{ij} is the Madelung contribution to the total potential, which is readily evaluated as $1/R_{ij}$ for a molecular compound or computed with an Ewald summation for a crystalline network [98].

$$\begin{aligned}M_{ij}&=\frac{\pi}{V}\sum_{\substack{\mathbf{h}=h\mathbf{a}^*+k\mathbf{b}^*+h\mathbf{c}^*\neq 0\\ \mathbf{x}=x\mathbf{a}+y\mathbf{b}+z\mathbf{c}}}\frac{\exp[2\pi\mathbf{h}(\mathbf{x}_j-\mathbf{x}_i)]}{|\mathbf{h}|^2}\exp\left(\frac{\pi^2|\mathbf{h}|^2}{K^2}\right)+\sum_{\substack{\mathbf{l}=u\mathbf{a}+v\mathbf{b}-w\mathbf{c}\neq 0\\ \mathbf{x}=x\mathbf{a}-y\mathbf{b}+z\mathbf{c}}}\\&\quad\times\frac{\operatorname{erfc}(K|\mathbf{l}+\mathbf{x}_j-\mathbf{x}_i|)}{|\mathbf{l}+\mathbf{x}_j-\mathbf{x}_i|}-\frac{2K}{\sqrt{\pi}}\delta_{ij}\quad \textit{with}\ \operatorname{erfc}(x)\\&=\frac{2}{\sqrt{\pi}}\int_x^{+\infty}\exp(-t^2)\,dt\end{aligned}$$

Here, V is the unit-cell volume and K is an adjustable parameter ruling the convergence speed of this double summation process.

Eq. (A.7) allows us to switch very quickly between a set of chemical parameters (electronegativities, sizes and atomic spatial positions) and the associated partial charge distribution q_i. From this distribution, it is possible to define two electrostatic balances (EB):

$$\begin{aligned}\mathrm{EB}&=\frac{e^2}{8Z\pi\epsilon_0}\sum_{i=1}^{n}\sum_{j=1}^{n}M_{ij}(K)(q,z)_i(q,z)_j\\&=\frac{694.68}{Z}\sum_{i=1}^{n}\sum_{j=1}^{n}M_{ij}(K)\,[\text{Å}^{-1}](q,z)_i(q,z)_j\ \text{kJ mol}^{-1},\end{aligned}$$

one using the partial charge distribution q_i, called the PEB (partial EB); and the other called the FEB (full EB), using integral oxidation states z_i. The ratio of these two balances defines the global ionicity I of the structure: $I(\%)=100\sqrt{\mathrm{PEB/FEB}}$.

The Madelung tensor M_{ij} allows also to get a set of strictly positive numbers $f_i=\partial^2E/\partial q_i\partial v_i\Leftrightarrow\partial\rho_{\mathrm{HOMO/LUMO}}/\partial N$, called frontier indexes [99], showing where the variation of μ_e should be largest [100]:

$$\eta=\frac{e}{4\pi\epsilon_0 r_i}f_i+\frac{1}{4\pi\epsilon_0}\sum_{j=1}^{n}M_{ij}f_j \quad \forall i=1,\ldots,n \quad \text{and} \sum_{i=1}^{n}f_i=1, \tag{A.8}$$

where η is the global hardness of the system, i.e. its HOMO–LUMO gap. The evaluation of these frontier indexes will not be considered in this paper.

The charge distributions reported in this paper have all been computed with the following parametrization for oxygen atoms: $\chi_O^0 = 9.63$ eV (electronegativity of 2p atomic orbitals) and $r_O = 73$ pm (single covalent radius). Other electronegativity and radii values are gathered in Table 12. Sometimes the partial charge q of an atom may be found to be greater than its maximum oxidation state z. In such a case, the radius of the atom was reduced (i.e. we have increased its hardness) until the $q = z$ condition was met. We have not tried to make any further adjustments as we are mainly interested in relative charge variations $\Delta q/q$ rather than reproducing charge distributions obtained by other methods. To obtain the charge distribution from a crystalline or molecular structure, we have written C++ software running under the Microsoft Windows environment. This software is able to perform the following tasks typically involved in any retrosynthesis:

(1) reading atomic coordinate files coming from crystal structure databases (Cambridge FDAT, Karlsruhe TXT, Broohaven PDB and Home-made TXT);

Table 12

Electronegativities and atomic sizes used in this work for computing partial charge distributions. For some atoms it has been necessary to adjust the size according to the crystalline environment in order to avoid charges higher than the well-known maximum oxidation state of the element

Atom	Mulliken electronegativity χ (eV)	Size (pm)
H	7.176	37
Li	3.010	123
Be	2.910	117–118
B	4.360	90
O	9.630	73
F	12.202	72
Na	1.640	112–154
Mg	2.310	145
Al	3.990	130
Si	7.295	118
Cl	9.350	99
K	1.620	140
Ca	2.110	163–198
Sc	5.620	144
Ti	5.514	136
Mn	6.601	117
Fe	6.878	125
Cu	1.480	138
Y	3.410	162
Zr	4.500	148
Ag	1.340	153
Sb	5.080	138
Cs	1.480	140
Ba	1.810	177–192
Sm	1.960	162
Gd	2.020	162
Er	2.040	158
Yb	1.850	170

(2) generating atomic fragments (up to 2500 atoms) from the imported crystal structure and saving the coordinates for visualization;
(3) visualizing and manipulating the fragment on the computer screen, including all the necessary functions for getting distances, angles and coordination spheres composition;
(4) computing the Madelung tensor through direct summation (fragments) or using the Ewald procedure (networks);
(5) solving a linear system of $(n+l)$ equations to obtain the partial charges q_i and the mean electronegativity $\langle\chi\rangle$, knowing the Madelung tensor, and a set of electronegativities and atomic radii; and
(6) producing an output file for a ray-tracing software for a good rendering of the 3D topologies of the fragments. All the drawings in this paper were made using the "Bob" ray-tracing software written by Watkins et al. [101].

References

[1] C.J. Brinker, G.W. Scherer, Sol–Gel Science: The Physics and Chemistry of Sol–Gel Processing, Academic Press, New York, 1990.
[2] J.P. Jolivet, De la Solution à L'Oxyde, Savoirs Actuels, Interéditions/CNRS Éditions, Paris, 1994.
[3] C. Magnier, Synthèse d'oxydes à morphologie contrôlée, Informations Chimie, vol. 366, 1995.
[4] J. Livage, M. Henry, C. Sanchez, Sol–gel chemistry of transition metal oxides, Prog. Solid State Chem. 18 (1988) 259–342.
[5] M. Henry, J.P. Jolivet, J. Livage, Aqueous chemistry of metal cations: hydrolysis, condensation and complexation, Struct. Bonding 77 (1992) 153–206.
[6] S. Doeuff, M. Henry, J. Livage, Sol–gel synthesis and characterization of titanium oxoacetate polymers, Mater. Res. Bull. 25 (1990) 1519–1529.
[7] C. Bonhomme, M. Henry, J. Livage, Complexing mercuric oxide sols by acetone, J. Non-Cryst. Solids 159 (1993) 22–30.
[8] J. Livage, M. Henry, J.P. Jolivet, C. Sanchez, Chemical synthesis of fine powders, Mater. Res. Soc. Bull. 15 (1990) 15–25.
[9] G. Férey, Oxyfluorinated microporous compounds ULM-n: chemical parameters, structures and a proposed mechanism for their molecular tectonics, J. Fluorine Chem. 72 (1995) 187–193.
[10] M. Estermann, L.B. McCusker, C. Baerlocher, A. Merrouche, H. Kessler, A synthetic gallophosphate molecular sieve with a 20-tetrahedral-atom pore opening, Nature 352 (1991) 320–322.
[11] A. Müller, E. Krickemeyer, J. Meyer, H. Bögge, F. Peters, W. Plass, E. Diemann, S. Dillinger, F. Nonnenbruch, M. Randerath, C. Menke, $[Mo_{156}(NO)_{14}O_{420}(OH)_{28}(H_2O)_{70}]^{(25\pm5)-}$: a water-soluble big wheel with more than 700 atoms and a relative molecular mass of about 24 000, Angew. Chem., Int. Ed. Engl. 34 (1995) 2122–2124.
[12] C. Sanchez, F. Ribot (Eds.), Proceedings of the First European Workshop on Hybrid Organic–Inorganic Materials, New J. Chem. 18 (1994).
[13] A. Müller, H. Reuter, S. Dillinger, Supramolecular inorganic chemistry: small guests in small and large hosts, Angew. Chem., Int. Ed. Engl. 34 (1995) 2328–2361.
[14] R.G. Parr, W Yang, Density functional approach to the frontier-electron theory of chemical reactivity, J. Am. Chem. Soc. 106 (1984) 4049–4050.
[15] H. Gamsjäger, R.K. Murmann, Oxygen-l8 exchange studies of aqua- and oxo ions, Adv. Inorg. Bioinorg. Mechanisms 2 (1983) 317–380.
[16] M. Eigen, Proton transfer and general acid–base catalysis in fast reactions and primary processes in chemical kinetics, Proceedings of the 5th Nobel Symposium, Interscience, New York, 1967, pp. 245–253.

[17] H. Krüger, Techniques for the kinetic study of fast reactions in solution, Chem. Soc. Rev. 11 (1982) 227–255.

[18] M. Ardon, A. Bino, Struct. Bonding 65 (1987) 1.

[19] H. Wendt, Die Kinetik typischer Hydrolysereactionen von mehrwertigen Kationen, Chimia 27 (1973) 575–588.

[20] P. Moore, S.F.A. Kettle, R.G. Wilkins, The kinetics of the general base hydrolysis of the dichromate anion, Inorg. Chem. 5 (1966) 220–222.

[21] J.H. Swinehart, G.W. Castellan, The kinetics of the chromate–dichromate reaction as studied by a relaxation method, Inorg. Chem. 3 (1964) 278–280.

[22] D.H. Doughty, R.A. Assink, B.D. Kay, Hydrolysis and condensation kinetics of dimeric sol–gel species by ^{29}Si NMR spectroscopy, Adv. Chem. Ser. 224 (1990) 241–249.

[23] G. Engelhardt, D. Hoebbel, ^{29}Si NMR spectroscopy reveals dynamic $[SiO_4]^{4-}$ group exchange between silicate anions in aqueous alkaline silicate solutions, J. Chem. Soc., Chem. Commun. (1984) 514–516.

[24] C.J. Creswell, R.K. Harris, P.T. Jageland, Exchanges rates between silicate anions in alkaline aqueous solution, J. Chem. Soc., Chem. Commun. (1984) 1261–1263.

[25] C.T.G. Knight, R.J. Kirkpatrick, E. Oldfield, The unexpectedly slow approach to thermodynamic equilibrium of the silicate anions in aqueous tetramethylammonium silicate solutions, J. Chem. Soc., Chem. Commun. (1986) 66–67.

[26] S.D. Kinrade, T.W. Swaddle, ^{29}Si NMR studies of aqueous silicate solutions. 2. Transverse ^{29}Si relaxation and the kinetics and mechanism of silicate polymerization, Inorg. Chem. 27 (1988) 4259–4264.

[27] C.T.G. Knight, A.R. Thompson, A.C. Kunwar, H.S. Gutowsky, E. Oldfield, R.J. Kirkpatrick, ^{17}O NMR spectroscopic studies of aqueous alkaline silicate solutions, J. Chem. Soc. Dalton Trans. (1989) 275–281.

[28] S. Sjöberg, L.O. Ohman, N. Ingri, Equilibrium and structural studies of silicon(IV) and aluminium(III) in aqueous solutions. 11. Polysilicate formation in alkaline aqueous solutions. a combined potentiometric and ^{29}Si NMR study, Acta Chem. Scand. A39 (1985) 93–107.

[29] R.L. Schmid, J. Felsche, G.J. Mclntyre, Location and anisotropic refinement of deuterium atoms in deuterium sodium silicate-deuterium oxide (1/8) $Na_2D_2SiO_4.8D_2O$ by neutron diffraction hydrogen bonding at 173 K, Acta Crystallogr. 40 (1984) 733–736.

[30] M. Henry, Application of the partial charge model to the aqueous chemistry of silica and silicates, Top. Mol. Org. Eng. 15 (1997) 273–334.

[31] R. Bianchi, T. Pliati, V. Diella, C.M. Gamaccioll, G. Mannucci, A re-examination of thortveitite, Am. Mineral. 73 (1988) 601–607.

[32] Yu.I. Smolin, Yu.F. Shepelev, Structure determination of erbium pyrosilicate, Izvs. Akad. Nauk. SSSR. Neorg. Mater. 4 (1968) 1133–1136.

[33] Yu.I. Smolin, Yu.F. Shepelev, I.K. Butikova, Crystal structure of ytterbium pyrosilicate, Zh. Struk. Khim. 12 (1971) 272–276.

[34] H. Voellenkle, A. Wittmann, H. Nowotny, The crystal structure of the compound $Li_6Si_2O_7$, Monatsh. Chem. 100 (1969) 295–303.

[35] J. Janczak, K. Kublak, T. Glowlak, Structure of barium copper pyrosilicate at 30O K, Acta Crystallogr. C 46 (1990) 1383-1385.

[36] Yu.I. Smolin, Yu.F. Shepelev, The determination of the structure of gadolinium pyrosilicate, Izv. Akad. Nauk SSSR Neorg. Mater. 3 (1967) 1034–1038.

[37] H.W. Dias, F.P. Glasser, R.P. Gurwardane, R.A. Howie, The crystal structure of δ-yttrium pyrosilicate, Z. Kristallogr. 191 (1990) 117–123.

[38] M. Kitama, N. Li, The crystal structure of synthetic akermanite $Ca_2MgSi_2O_7$, Neues J. Miner. 1981 (1981) 1–10.

[39] S. Saburi, I. Kusachi, C. Henmi, A. Kawahara, I. Kawada, Refinement of the structure of rankinite, Miner. J. 8 (1976) 240–246.

[40] Yu.I. Smolin, Yu.F. Shepelev, I.K. Butikova, The crystal structure of the low-temperature form of samarium pyrosilicate, Kristallografiya 15 (1970) 256–261.

[41] P.D. Robinson, J.H. Fang, Barylite, $BaBe_2Si_2O_7$: its space group and crystal structure, Am. Mineral. 62 (1977) 167–169.

[42] R.D. Shannon, Revised effective ionic radii and systematic studies of interatomic distances in halides and chalchogenides, Acta Crystallogr. A 32 (1976) 751–766.

[43] T.P. Kouznetsova, N.N. Nevskii, V.V. Ilioukhine, N.V. Belov, Crystal structure determination of a Na,Ca-triorthosilicate $Na_2Ca_3[Si_3O_{10}]$, Kristallografiya 25 (1980) 855–857.

[44] H.F.W. Taylor, The crystal structure of kilchoanite, $Ca_6(SiO_4)(Si_3O_{10})$, with some comments on related phases, Mineral. Mag. 38 (1971) 26–31.

[45] G. Donnay, R. Allman, Si_3O_{10} groups in the crystal structure of ardennite, Acta Crystallogr. B 24 (1968) 845–855; B 27 (1971) 1871–1875.

[46] M. Jansen, H.L. Keller, $Ag_{10}Si_4O_{13}$, das erste Tetrasilikat, Angew. Chem. 91 (1979) 500.

[47] K. Heidebrecht, M. Jansen, $Ag_{18}(SiO_4)_2(Si_4O_{13})$, the first silver silicate with mixed anions, Z. Anorg. Allg. Chem. 597 (1991) 79–86; 606 (1991) 242.

[48] R.K. Harris, J. Jones, C.T.G. Knight, Silicon-29 studies of aqueous silicate solutions Part II. Isotopic enrichment, J. Mol. Struct. 69 (1980) 95–103.

[49] S.D. Kinrade, T.W. Swaddle, Silicon-29 NMR studies of aqueous silicate solutions. 1 Chemical shifts and equilibria, Inorg. Chem. 27 (1988) 4253–4259.

[50] S. Sasaki, K. Fujino, Y. Takeuchi, R. Sadanaga, On the estimation of atomic charges by the X-ray method for some oxides and silicates, Acta Crystallogr. A 36 (1980) 904–915.

[51] S. Sasaki, Y. Takeuchi, K. Fujino, S. Akimoto, Electron-density distributions of three orthopyroxenes $Mg_2Si_2O_6$, $CO_2Si_2O_6$ and $Fe_2Si_2O_6$, Z. Kristallogr. 158 (1982) 279–297.

[52] Y. Ohashi, L.W. Finger, The effect of Ca substitution on the structure of clinoenstatite, Carnegie Institution of Washington: Yearbook 75 (1976) 743–746.

[53] Y. Ohashi, Polysynthetically-twinned structures of enstatite and wollastonite, Phys. Chem. Mineral. 10 (1984) 217–229.

[54] K.-F. Hesse, Refinement of the crystal structure of wollastonite-2M (parawollastonite), Z. Kristallogr. 168 (1984) 93–98.

[55] Y. Ohashi, L.W. Finger, Pyroxenoids. A comparison of refined structures of rhodonite and pyroxmangite, Carnegie Institution of Washington: Yearbook 74 (1975) 564–569.

[56] C. Pagnoux, A. Verbaere, Y. Piffard, M. Tournoux, $CsSbO(SiO_3)_2$; a new $\{uB,1^{1}_{\infty}\}[^{12}SiO_3]$ chain silicate, Acta Crystallogr. C 47 (1991) 2297–2299.

[57] M. Cameron, G.V. Gibbs, The crystal structure and bonding of fluor-tremolite: a comparison with hydroxyl tremolite, Am. Mineral. 58 (1973) 879–888.

[58] T. Yamanaka, H. Mori, The structure and polytypes of α-$CaSiO_3$ (pseudowollastonite), Acta Crystallogr. B 37 (1981) 1010–1017.

[59] K. Fisher, Crystal structure determination of benitoite $BaTi(Si_3O_9)$, Z. Kristallogr. 129 (1969) 222–243.

[60] V.A. Blinov, N.G. Shumyatskaya, A.A. Voronkov, V.V. Ilyukhin, N.V. Belov, Refinement of the crystal structure of wadeite $K_2Zr(Si_3O_9)$ and its relation to kindred structural types, Kristallografiya 22 (1977) 59–65.

[61] J. Janczak, R. Kubiak, Structure of the cyclic barium copper silicate $Ba_2Cu_2[Si_4O_{12}]$ at 300 K, Acta Crystallogr. C 48 (1992) 8–1O.

[62] I. Hassan, H.D. Grundy, The crystal structure and thermal expansion of tugtupite $Na_8(Al_2Be_2Si_8O_{24})Cl_2$, Can. Mineral. 29 (1991) 385–390.

[63] L.A. Groat, F.C. Hawthome, Refinement of the structure of papagoite, $CaCuAlSi_2O_6(OH)_3$, Mineral. Petrol. 37 (1987) 89–96.

[64] W. Hilmer, The crystal structure of potassium acid metasilicate $K_4(HSiO_3)_4$, Acta Crystallogr. 17 (1964) 1063–1066; 18 (1965) 574.

[65] C. Pagnoux, A. Verbaere, Y. Kanno, Y. Piffard, M. Tournoux, The synthesis and crystal structures of novel antimony compounds: $A_4Sb_4O_8(X_4O_{12})$ (A:K, Rb, Cs, Tl; X = Si,Ge), J. Solid State Chem. 99 (1992) 173–181.

[66] B. Morosin, Structure and thermal expansion of beryl, Acta Crystallogr. B 28 (1972) 1899–1903.

[67] M.J. Buerger, C.W. Burnham, D.R. Peacor, Assessment of the several structures proposed for tourmaline, Acta Crystallogr. 15 (1962) 583–590.

[68] R. Barton, Jr, Refinement of the crystal structure of buergerite and the absolute orientation of tourmalines, Acta Crystallogr. B 25 (1969) 1524–1533.

[69] S.J. Lippard, Oxo-bridged polyiron centers in biology and chemistry, Angew. Chem., Int. Ed. Engl. 27 (1988) 344–361.

[70] N.V. Belov, B.A. Maksimov, Y.Z. Nozik, L.A. Muradyan, The refinement of the crystal structure of dioptase $CU_6(Si_6O_{18})(H_2O)_6$ by the X-ray and neutron diffraction methods, Dokl. Akad. Nauk SSSR 239 (1978) 842–845.

[71] K.H. Breuer, W. Eysel, R. Müller, Structural and chemical varieties of dioptase $CU_6[Si_6O_{18}].6H_2O$. II Structural properties, Z. Kristallogr. 187 (1989) 15–23.

[72] V.V. Ilyukhin, N.V. Belov, The crystal structure of lovozerite, Dokl. Akad. Nauk SSSR 131 (1960) 176–179.

[73] N.M. Chernitsova, Z.V. Pudovkina, A.A. Voronkov, V.V. Ilyukhin, Y.A. Pyatenko, Imandrite $Na_{12}Ca_3Fe_2(Si_6O_{18})_2$ a representative of a new branch in the lovozerite structural family, Dokl. Akad. Nauk SSSR 252 (1980) 618–621.

[74] A.A. Khan, W.H. Baur, Eight-membered cyclosilicate rings in muirite, Science 173 (1971) 916–918.

[75] V.M. Golyshev, V.I. Simonov, N.V. Belov, Crystal structure of eudialite, Kristallografiya 16 (1971) 93–98.

[76] Yu.I. Smolin, New silicate complex Si_6O_{15} in the crystal $[Ni(en)_3]Si_2O_5$. 8,7 H_2O, Kristallografiya 15 (1970) 31–37.

[77] Yu.I. Smolin, Yu.F. Chepelev, R. Pomec, D. Hoebbel, W. Wieker, Crystal structure determination of the tetramethylammonium silicate $8[N(CH_3)_4]Si_8O_{20}$.64,8 H_2O at −100 °C, Kristallografia 24 (1979) 38–44.

[78] G.O. Brunner, W.M. Meier, Framework density distribution of zeolite-type tetrahedral nets, Nature 337 (1989) 146–147.

[79] F.C. Hawthorne, M. Kimata, P. Cerny, N. Ball, G.R. Rossman, J.D. Grice, The crystal chemistry of the milarite-group minerals, Am. Mineral. 76 (1991) 1836–1856.

[80] P. Politzer, H. Weinstein, Some relations between electronic distribution and electronegativity, J. Chem. Phys. 71 (11) (1979) 4218–4220.

[81] L. Pauling, The nature of the chemical bond. IV. The energy of single bonds and the relative electronegativity of atoms, J. Am. Chem. Soc. 54 (1932) 3570–3582.

[82] R.T. Sanderson, An interpretation of bond length and a classification of bonds, Science 114 (1951) 670–672.

[83] R.G. Parr, R.A. Donnelly, L. Levy, W.E. Palke, Electronegativity: the density functional viewpoint, J. Chem. Phys. 68 (8) (1978) 3801–3807.

[84] R.G. Pearson, Hard and soft acids and bases HSAB. Parts I and II, J. Chem. Ed. 45 (1963) 581–587.

[85] R.F. Nalewajski, Electrostatic effects in interactions between hard (soft) acids and bases, J. Am. Chem. Soc. 106 (1984) 944–945.

[86] L. Komorowski, Empirical evaluation of chemical hardness, Chem. Phys. Lett. 134 (6) (1987) 526–540.

[87] R.S. Mulliken, A new electroaffinity scale; together with data on valence states and on valence ionization potentials and electron affinities, J. Chem. Phys. 2 (1934) 782–793.

[88] E.C.M. Chen, W.E. Wentworth, J.A. Alaya, The relationship between the mulliken electronegativities of the elements and the work functions of metals and nonmetals, J. Chem. Phys. 67 (6) (1977) 2642–2647.

[89] R.T. Poole, D.R. Williams, J.D. Riley, J.G. Jenkin, J. Liesegang, R.C.G. Leckey, Electronegativity as a unifying concept in the determination of Fermi energies and photoelectric thresholds, Chem. Phys. Lett. 36 (1975) 401–403.

[90] R.G. Pearson, Hard and soft acids and bases—the evolution of a chemical concept, Coord. Chem. Rev. 100 (1990) 403–425.

[91] D.W. Davis, D.A. Shirley, T.D. Thomas, X-ray photoelectron spectroscopy of fluorinated benzenes, J. Am. Chem. Soc. 94 (1972) 6565–6575.

[92] R.G. Pearson, Absolute electronegativity and absolute hardness of Lewis acids and bases, J. Am. Chem. Soc. 107 (1985) 6801–6806.

[93] W.J. Mortier, S.K. Ghosh, S. Shankar, Electronegativity equalization method for the calculation of atomic charges in molecules, J. Am. Chem. Soc. 108 (1986) 4315–4320.

[94] D.E. Parry, Determination of atomic partial charges using X-ray photoelectron spectroscopy application to crystalline solids, J. Chem. Soc., Faraday Trans. II 70 (1974) 337–345.

[95] K.A. Van Genechten, W.J. Mortier, P. Geerlings, Framework electronegativity: a novel concept in solid-state chemistry, J. Chem. Phys. 86 (1987) 5063–5071.

[96] S.G. Bratsch, Revised Mulliken electronegativities, J. Chem. Ed. 65 (1988) 34–41.

[97] H. Basch, A. Viste, H.B. Gray, Valence orbital ionization potentials from atomic spectral data, Theor. Chim. Acta (Berlin) 3 (1965) 458–464.

[98] R. Fischer, H. Ludwiczek, Computer programs for the calculation of Madeluna constants and their recalculation for spinel type, Monatsh. Chem. 106 (1975) 223–228.

[99] R.G. Parr, W. Yang, Density functional approach to the frontier-electron theory of chemical reactivity, J. Am. Chem. Soc. 106 (1984) 4049–4050.

[100] B.G. Baekelandt, W.J. Mortier, R.A. Schoonheydt, The EEM approach to chemical hardness in molecules and solids: fundamentals and applications, Struct. Bonding 80 (1993) 187–227.

[101] C.D. Watkins, S.B. Coy, M. Finlay, Photorealism and Ray Tracing in C, M&T Publishing, San Mateo, 1992.